

# Atomistic simulations, mesoscopic modeling, and theoretical analysis of thermal conductivity of bundles composed of carbon nanotubes

Alexey N. Volkov,<sup>a)</sup> Richard N. Salaway, and Leonid V. Zhigilei<sup>b)</sup>  
*Department of Materials Science and Engineering, University of Virginia, 395 McCormick Road,  
 Charlottesville, Virginia 22904-4745, USA*

(Received 21 June 2013; accepted 14 August 2013; published online 10 September 2013)

The propensity of carbon nanotubes (CNTs) to self-organize into continuous networks of bundles has direct implications for thermal transport properties of CNT network materials and defines the importance of clear understanding of the mechanisms and scaling laws governing the heat transfer within the primary building blocks of the network structures—close-packed bundles of CNTs. A comprehensive study of the thermal conductivity of CNT bundles is performed with a combination of non-equilibrium molecular dynamics (MD) simulations of heat transfer between adjacent CNTs and the intrinsic conductivity of CNTs in a bundle with a theoretical analysis that reveals the connections between the structure and thermal transport properties of CNT bundles. The results of MD simulations of heat transfer in CNT bundles consisting of up to 7 CNTs suggest that, contrary to the widespread notion of strongly reduced conductivity of CNTs in bundles, van der Waals interactions between defect-free well-aligned CNTs in a bundle have negligible effect on the intrinsic conductivity of the CNTs. The simulations of inter-tube heat conduction performed for partially overlapping parallel CNTs indicate that the conductance through the overlap region is proportional to the length of the overlap for CNTs and CNT-CNT overlaps longer than several tens of nm. Based on the predictions of the MD simulations, a mesoscopic-level model is developed and applied for theoretical analysis and numerical modeling of heat transfer in bundles consisting of CNTs with infinitely large and finite intrinsic thermal conductivities. The general scaling laws predicting the quadratic dependence of the bundle conductivity on the length of individual CNTs in the case when the thermal transport is controlled by the inter-tube conductance and the independence of the CNT length in another limiting case when the intrinsic conductivity of CNTs plays the dominant role are derived. An application of the scaling laws to bundles of single-walled (10,10) CNTs reveals that the transition from inter-tube-conductance-dominated to intrinsic-conductivity-dominated thermal transport in CNT bundles occurs in a practically important range of CNT length from  $\sim 20$  nm to  $\sim 4$   $\mu\text{m}$ . © 2013 AIP Publishing LLC. [<http://dx.doi.org/10.1063/1.4819911>]

## I. INTRODUCTION

The emergence of novel approaches for thermal management at micro/nano scales is crucial for further advancement and miniaturization of microelectronic devices. Due to their high thermal conductivity<sup>1–5</sup> and large surface area, carbon nanotubes (CNTs) are considered as promising structural elements in the design of heat sinks for cooling of microprocessors and other microelectronic devices.<sup>6</sup> Examples of recent technological developments utilizing the unique thermal properties of CNTs include the use of vertically aligned arrays of CNTs as thermal interface materials<sup>7,8</sup> or micro-fins<sup>9,10</sup> to enhance the rate of the heat transfer from a microelectronic device to the surroundings.

In most CNT-based materials, such as CNT mats, films, buckypaper, and vertically aligned arrays, the van der Waals attraction between individual nanotubes results in their arrangement into bundles that form entangled continuous networks.<sup>11–16</sup> Recently, the structure of continuous

networks of CNT bundles was reproduced in simulations<sup>17</sup> performed with a mesoscopic model representing individual CNTs as chains of stretchable cylindrical segments<sup>18</sup> and accounting for the internal stretching, bending, and buckling of CNTs,<sup>17,18</sup> as well as the van der Waals interactions among the CNTs.<sup>19</sup> As one can see from Fig. 1, the simulated CNT networks have complex hierarchical structure, with bundles of CNTs serving as primary building blocks. In accord with experimental observations,<sup>11,12,20</sup> the CNTs exhibit partial close-packed hexagonal ordering in the bundles, Fig. 1(b), defined by the minimization of the potential energy of inter-tube interactions.

The formation of bundles has important implications for thermal transport properties of CNT materials. In particular, calculations of thermal conductivity of the networks of bundles predict the values of conductivity that are substantially, by about an order of magnitude, higher as compared to the values predicted for systems of the same density composed of randomly dispersed individual CNTs.<sup>21</sup> This enhancement is attributed to an efficient heat transfer along the continuous intertwined bundles that form the frameworks of the network structures. While a rigorous theoretical analysis of thermal conductivity of complex network structures characteristic of CNT materials is a challenging task, a major prerequisite for

<sup>a)</sup>Present address: Department of Mechanical Engineering, University of Alabama, 7th Avenue, Tuscaloosa, Alabama 35401, USA. Electronic mail: [avolkov1@ua.edu](mailto:avolkov1@ua.edu)

<sup>b)</sup>Author to whom correspondence should be addressed. Electronic mail: [lz2n@virginia.edu](mailto:lz2n@virginia.edu)

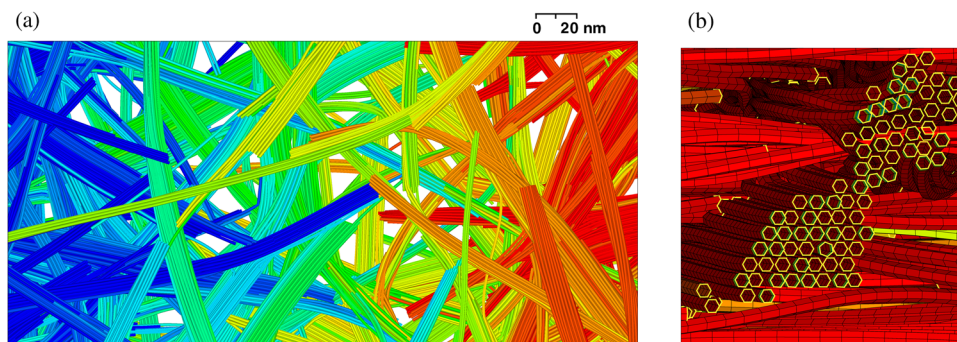


FIG. 1. Fragments of a continuous network of bundles generated in a mesoscopic simulation.<sup>17,21</sup> The network has density of  $0.2 \text{ g cm}^{-3}$  and is composed of 200 nm long (10,10) CNTs. In the system shown in panel (a), a temperature gradient is applied in the horizontal direction and individual nanotubes are colored by their temperatures. In panel (b), typical bundle cross sections with a partial hexagonal ordering of CNTs are shown.

addressing this challenge is a clear understanding of the thermal transport properties of the primary building blocks to the network structures—close-packed bundles of CNTs. The understanding of the thermal transport in individual bundles is also important for applications where CNT bundles are used as interconnects in microelectronic devices.<sup>22,23</sup>

The experimental values of conductivity of CNT bundles,  $k_b$ , span a discouragingly broad range, from less than  $10 \text{ Wm}^{-1}\text{K}^{-1}$  (e.g., Refs. 24 and 25) up to more than a thousand of  $\text{Wm}^{-1}\text{K}^{-1}$  (Ref. 1). The large variability of the experimental values may be attributed to the differences in the measurement techniques, thickness, packing density, and structural parameters of the bundles, concentration of intrinsic defects in the CNTs and inter-CNT crosslinks, as well as inclusions of graphitic fragments, residual solvent, or catalyst nanoparticles. The lowest values of  $3\text{--}9 \text{ Wm}^{-1}\text{K}^{-1}$  are reported for relatively thick (on the order of  $100 \mu\text{m}$ ) “bundles” of multi-walled CNTs with packing density that is typical for vertically aligned arrays of CNTs.<sup>24,25</sup> Higher thermal conductivity up to  $253 \text{ Wm}^{-1}\text{K}^{-1}$  is measured by a non-contact two-laser optical technique for thin (10–12 nm in diameter) bundles consisting of 4–7 single-walled CNTs.<sup>26,27</sup> Similar room-temperature conductivity of  $\sim 150 \text{ Wm}^{-1}\text{K}^{-1}$  is obtained for a 10 nm bundle of single-walled CNTs by contact measurements performed on a microfabricated device in Ref. 28, although a very low value of several  $\text{Wm}^{-1}\text{K}^{-1}$  is reported in this work for a thicker bundle of 148 nm in diameter. The conductivity measured in Ref. 29 for dense bundles consisting of tens to hundreds of well-aligned multi-walled CNTs (diameter of up to 200 nm) is found to drop from about 400 to  $150 \text{ Wm}^{-1}\text{K}^{-1}$  as the thickness of the bundle increases. Even stronger thickness dependence is observed for bundles of multi-walled CNTs in Ref. 1, where the room-temperature thermal conductivity is reported to drop from  $\sim 1200 \text{ Wm}^{-1}\text{K}^{-1}$  to  $\sim 250 \text{ Wm}^{-1}\text{K}^{-1}$  as the bundle diameter increases from 80 to 200 nm.

The decrease of the thermal conductivity with increasing number of CNTs in the bundles<sup>1,28,29</sup> and, more generally, much lower thermal conductivity of bundles as compared to individual CNTs (experiments performed for suspended CNTs yield room temperature values that are ranging from  $1400 \text{ Wm}^{-1}\text{K}^{-1}$  to  $3000 \text{ Wm}^{-1}\text{K}^{-1}$  for multi-walled CNTs<sup>1,2,4,5</sup> and even higher values for single-walled CNTs<sup>3,4</sup>) are commonly attributed to the van der Waals inter-tube interactions in the bundles and associated

enhanced phonon scattering.<sup>27–31</sup> The reduction of the intrinsic thermal conductivity of CNTs and other carbon structures due to the non-bonding interactions in materials that consist of multiple structural elements was suggested by Berber *et al.*<sup>32</sup> based on the results of atomistic Green-Kubo calculations of thermal conductivity. This suggestion, however, while echoed in a number of works, e.g., Refs. 28–31, 33, is only a conjecture extrapolated from the computational prediction on the difference between the thermal conductivity of a graphene monolayer and graphite. An opposite notion of a weak effect of the interactions of perfect (defect-free) CNTs in a bundle on thermal conductivity, which can be substantially enhanced by structural defects, has been put forward in Ref. 34 based on the kinetic model calculations of thermal conductivity. Thus, one of the goals of the simulations reported in the present paper is to clarify the question on the effect of the inter-tube coupling in CNT bundles on the intrinsic thermal conductivity of the CNTs.

Another important factor that defines the thermal conductivity of a bundle composed of CNTs that are shorter than the total length of the bundle is the presence of CNT ends that interrupt the fast heat flow in individual CNTs and necessitate the much slower heat exchange between the CNTs. In this case, one can expect the thermal conductivity of a bundle to be limited by the weak thermal coupling between the CNTs<sup>35–42</sup> rather than the heat conduction within the individual CNTs. The dependence of the thermal conductivity of bundles on the intrinsic conductivity of CNTs and the inter-tube conductance in the overlap regions between the adjacent CNTs has not been discussed in literature so far.

In this paper, we report the results of a thorough investigation of the thermal conductivity of CNT bundles performed by a combination of a non-equilibrium molecular dynamics (MD) simulation study of the heat transfer between adjacent CNTs and the intrinsic conductivity of CNTs in a bundle with a theoretical analysis leading to the design of a robust model capable of predicting the thermal conductivity of a bundle based on the properties of constituent CNTs and structural parameters of the bundle. The results of MD simulations, presented in Sec. II, suggest that (1) contrary to the widespread notion of strongly reduced conductivity of CNTs in bundles,<sup>27–32</sup> the van der Waals interactions between defect-free well-aligned CNTs in a bundle have negligible effect on the intrinsic conductivity of the

CNTs and (2) for sufficiently long parallel nanotubes the conductance through the overlap region between the neighboring CNTs is proportional to the length of the overlap. Based on the predictions of the atomistic simulations, we then develop a mesoscopic-level model of heat transfer in CNT bundles (Sec. III) and apply this model for theoretical and numerical analysis of thermal conductivity of bundles consisting of CNTs with infinitely large and finite intrinsic thermal conductivities (Secs. IV and V, respectively). Because of the general nature of the mesoscopic model, the results of the analysis are applicable not only to bundles of CNTs but also to bundles composed of any type of heat conducting nanofibers. The general scaling laws predicting the quadratic dependence of the bundle conductivity on the length of individual CNTs in the case when the thermal transport is controlled by the inter-tube conductance and the independence of the CNT length in another limiting case when the intrinsic conductivity of CNTs plays the dominant role are derived in Secs. IV and V. The application of these scaling laws to bundles of single-walled (10,10) CNTs in Sec. VI reveals that the transition from inter-tube-conductance-dominated to intrinsic-conductivity-dominated thermal transport in CNT bundles occurs in a practically important range of CNT length from  $\sim 20$  nm to  $\sim 4$   $\mu\text{m}$ .

## II. ATOMISTIC SIMULATIONS OF CNT CONDUCTIVITY AND INTER-TUBE CONDUCTANCE IN BUNDLES

Two series of non-equilibrium MD simulations are performed in order to reveal the basic mechanisms of heat transfer in bundles of CNTs. In the first series of simulations, the effect of inter-tube coupling on the intrinsic thermal conductivity of the CNTs is investigated by comparing conductivities of a single CNT, a pair of parallel CNTs, and a bundle composed of 7 hexagonally packed CNTs. In the second series of simulations, the conductance of an overlap region between a pair of parallel CNTs is studied as a function of the overlap length. In both series, the simulations are performed for (10,10) single-walled CNTs using the LAMMPS package.<sup>43</sup> The LAMMPS implementation of the AIREBO potential<sup>44</sup> is used to describe the interatomic interactions. This implementation adopts the 2nd generation REBO potential<sup>45</sup> for chemically bonded carbon atoms within the CNTs and describes the van der Waals interactions between non-bonded carbon atoms by the Lennard-Jones potential with parameters  $\sigma = 3.40$   $\text{\AA}$  and  $\varepsilon = 2.84$  meV. A cutoff function that ensures a smooth transition of the Lennard-Jones potential to zero is applied in a range of interatomic distances from  $2.16\sigma$  to  $3\sigma$ .<sup>44,46</sup>

### A. Conductivity of a CNT in a bundle

The effect of the inter-tube interactions on the intrinsic conductivity of a nanotube is investigated in MD simulations performed for systems of one, two, and seven (10,10) CNTs that are shown schematically in Fig. 2(a). The individual CNTs used in the simulations are 160 and 300 nm long and consist of 26 440 and 49 640 atoms, respectively. The CNTs are covered by 110-atom caps at the ends with one of the caps interfacing with the nanotube by a 20-atom ring

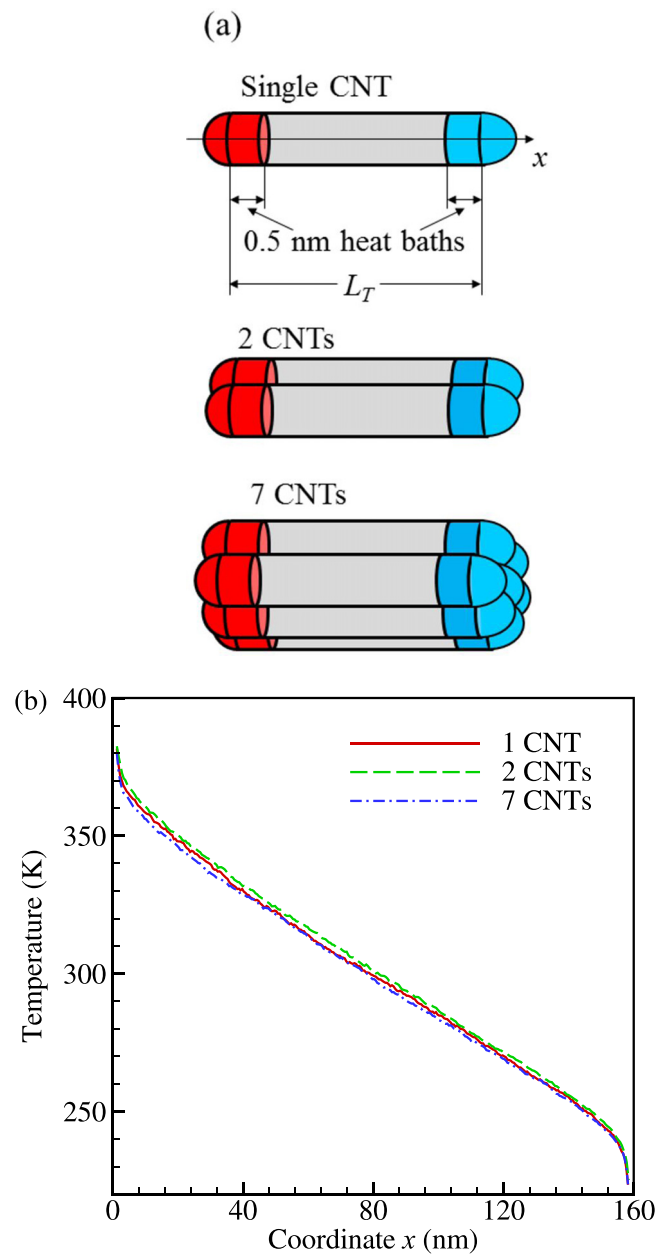


FIG. 2. A schematic representation (not to scale) of the three systems used in the MD simulation study of the effect of inter-tube coupling on the intrinsic thermal conductivity of CNTs in bundles (a) and representative temperature profiles obtained in the simulations performed for (10,10) CNTs of length  $L_T = 160$  nm (b). Heat flux is applied to each CNT individually and the values of thermal conductivity are obtained from the steady-state temperature profiles. All simulations are performed for capped CNTs with the cylindrical part of length  $L_T$ . The temperature profiles in panel (b) are obtained by averaging over the steady-state parts of the simulations and, for systems composed of 2 and 7 CNTs, by additional averaging of the profiles calculated for individual CNTs in the bundles.

constituting a half of the nanotube's unit cell. Free (vacuum) boundary conditions are applied in all directions. The configurations of CNT pairs and bundles are relaxed by quenching atomic velocities for 15 ps in order to establish a low-energy separation between the nanotubes and to prevent oscillations that would affect inter-tube interactions. All systems are then gradually heated to 300 K by applying the Langevin thermostat for 30 ps while ensuring that the total linear and angular

momenta are zero.<sup>47</sup> Finally, in order to establish a steady-state temperature gradient along the CNTs, a constant heat flux is applied by scaling the velocities of atoms in two 0.5 nm wide heat bath regions located on either end of each CNT, neglecting the hemispherical caps. The velocity scaling is done so that the same amount of energy,  $Q_{HB}$ , is added and removed per unit time in the two heat bath regions of each CNT. The rates of the energy addition/removal used in the simulations of 160 nm and 300 nm CNTs are  $Q_{HB} = 1.5 \text{ eV ps}^{-1}$  and  $Q_{HB} = 1.3 \text{ eV ps}^{-1}$ , respectively. These rates correspond to heat fluxes of  $Q_{HB}/A_T = 1.68 \times 10^{11} \text{ Wm}^{-2}$  and  $Q_{HB}/A_T = 1.46 \times 10^{11} \text{ Wm}^{-2}$ , where  $A_T$  is the cross-sectional area of a CNT defined as  $2\pi\delta_T R_T$ ,  $R_T = 0.67 \text{ nm}$  is the nanotube radius found in MD simulations of an isolated CNT equilibrated at 300 K, and  $\delta_T = 0.34 \text{ nm}$  is the nominal thickness of the CNT wall taken to be equal to the interlayer spacing in graphite.<sup>48–50</sup>

The values of thermal conductivity of individual CNTs,  $k_T$ , are calculated from the Fourier law,  $k_T = -Q_{HB}/(A_T dT/dx)$ , where the temperature gradients,  $dT/dx$ , are determined by linear fits of steady-state temperature profiles generated in constant heat flux simulations, e.g., Fig. 2(b). The  $\sim 20 \text{ nm}$  regions of non-linear temperature distributions in the vicinity of the CNT ends are excluded from the calculation of  $dT/dx$ . The time required for the establishment of the steady-state temperature profiles was about 0.4 ns for 160 nm CNTs and 0.8 ns for 300 nm CNTs. In the steady state, the simulations are run for an additional 200 ps to 1200 ps and the instantaneous values of thermal conductivity are evaluated every 5 fs from instantaneous temperature gradients. The instantaneous values of thermal conductivity collected in the steady-state regime are found to obey normal distributions, confirming the random statistical nature of the fluctuations of these values during the time span of the data collection. The average thermal conductivity  $k_T$  and the sample standard deviation are then calculated from the instantaneous values. For multi-tube configurations, the mean of the thermal conductivities and the pooled standard deviation are calculated for all CNTs present in a given configuration.

The temperature profiles shown in Fig. 2(b) for an isolated CNT and CNT bundles are almost identical, suggesting that the thermal conductivity of individual CNTs is not significantly affected by the interactions among the CNTs. Indeed, the values of  $k_T$  listed in Table I for each of the three configurations are within the standard deviations of each other for a given length of the CNTs, while the increase of

$k_T$  with increasing CNT length,  $L_T$ , is characteristic of the diffusive-ballistic phonon transport in CNTs that has been discussed in a number of works.<sup>47,48,51–53</sup>

The absence of any significant effect of the van der Waals inter-tube coupling in CNT bundles on the intrinsic thermal conductivity of individual CNTs is consistent with relatively small changes of the vibrational spectra of CNTs due to the inter-tube interactions and negligible contribution of inter-tube phonon modes to thermal conductivity of bundles.<sup>34,54</sup> It also suggests that three-phonon umklapp scattering involving phonons from neighboring CNTs does not play any significant role in perfect bundles consisting of defect-free CNTs. The results of the simulations, however, contradict the experimental observation of the pronounced decrease of the thermal conductivity of bundles with increasing bundle thickness<sup>1,28,29</sup> that is commonly attributed to the dramatic enhancement of phonon scattering by the inter-tube interactions.<sup>27–32</sup> An alternative explanation of the bundle thickness dependence of the thermal conductivity could be the higher degree of CNT misalignment and increased concentration of inter-tube defects, crosslinks, and foreign inclusions in larger bundles, which could result in the increase of both the phonon scattering and inter-tube contact thermal resistance. Indeed, SEM images of thick “bundles” that exhibit the lowest thermal conductivity on the order of several  $\text{Wm}^{-1}\text{K}^{-1}$  reveal a loose arrangement of poorly aligned CNTs that resemble pillars cut from vertically aligned arrays of CNTs.<sup>24,25</sup>

## B. Inter-tube conductance in CNT bundles

The dependence of the conductance at the interface between two partially overlapping parallel CNTs on the length of the overlap region is investigated in the second series of atomistic simulations. The computational setup used in these simulations is shown in Fig. 3(a). Periodic boundary conditions are used in the axial direction (along the  $x$ -axis), while free boundary conditions are applied in other directions. The two (10,10) CNTs have the same length of 100 or 200 nm and are covered by hemispherical caps at the ends. The length of the overlap region,  $\Delta x_{12}$ , is systematically varied in the range of 10 to 95 nm, leading to the corresponding variation of the size of the computational cell in the  $x$ -direction,  $L_x = 2L_T - 2\Delta x_{12}$ . Similar to the simulations discussed in Sec. II A, the initial systems are relaxed by quenching atomic velocities for 10 ps and brought to 300 K by applying the Langevin thermostat for 30 ps. A constant heat flux is then generated by scaling the velocities of atoms in two 2 nm wide heat bath regions defined in the centers of the two CNTs, so that the same amount of energy,  $Q_{HB} = 0.4 \text{ eV ps}^{-1}$  for 100 nm CNTs and  $Q_{HB} = 1 \text{ eV ps}^{-1}$  for 200 nm CNTs, is added and removed per unit time in the two heat bath regions, as shown in Fig. 3(a). The thermal energy is conducted from the center of the hot CNT, out to the overlap regions, across to the cold CNT by inter-tube conductance, and finally to the heat bath region in the center of the cold tube.

Steady-state temperature distributions are established in the simulations by the time of 1.5 to 4.5 ns, depending on the values of  $L_T$  and  $\Delta x_{12}$ . The simulations are continued in the

TABLE I. Thermal conductivities of a (10,10) CNT,  $k_T$ , and the corresponding standard deviations from the mean values predicted in MD simulations performed for a single CNT, a pair of parallel interacting CNTs, and a bundle of 7 CNTs. The configurations considered in the simulations are schematically represented in Fig. 2(a) and consist of CNTs with length of  $L_T = 160$  and 300 nm. For a given length of the CNTs, the values of  $k_T$  are within the standard deviations of each other, suggesting that the effect of the inter-tube coupling on the intrinsic thermal conductivity of CNTs is statistically insignificant.

$L_T$	Single CNT	2-CNT configuration	7-CNT configuration
160 nm	$223 \pm 15 \text{ Wm}^{-1}\text{K}^{-1}$	$220 \pm 14 \text{ Wm}^{-1}\text{K}^{-1}$	$215 \pm 9 \text{ Wm}^{-1}\text{K}^{-1}$
300 nm	$241 \pm 6 \text{ Wm}^{-1}\text{K}^{-1}$	$241 \pm 6 \text{ Wm}^{-1}\text{K}^{-1}$	$238 \pm 6 \text{ Wm}^{-1}\text{K}^{-1}$

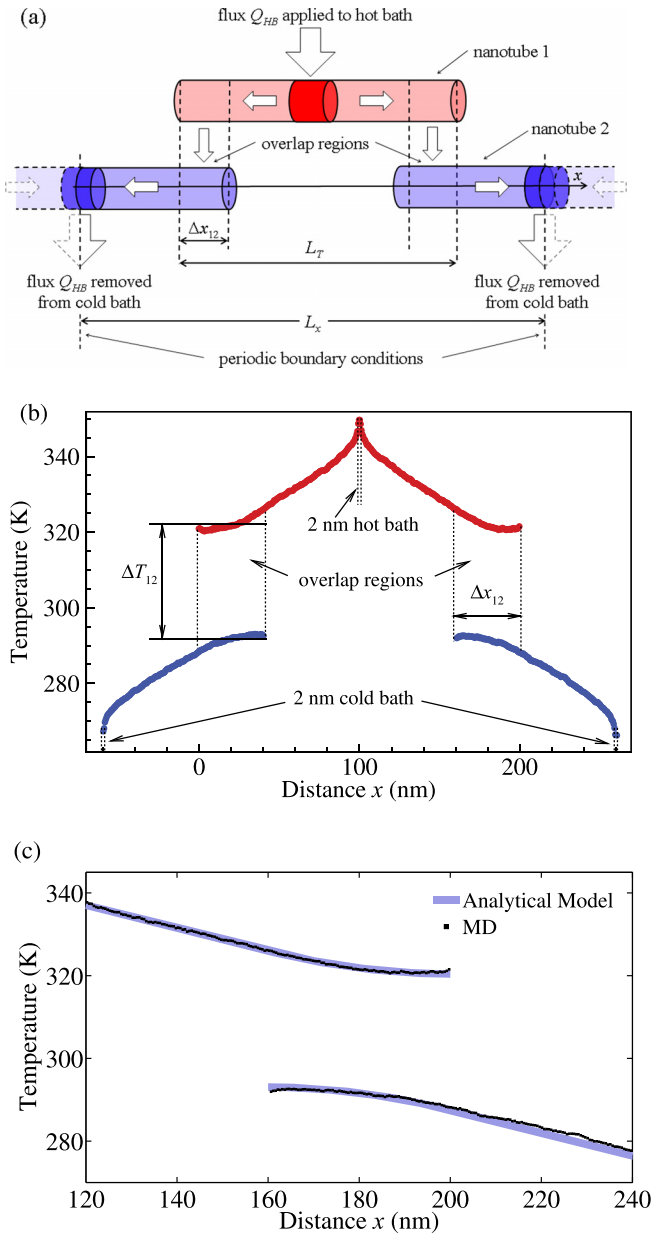


FIG. 3. Computational setup used in MD simulations of the conductance through overlap regions between parallel CNTs (a), a representative temperature distribution in the overlapping nanotubes 1 (red curve) and 2 (blue curve) obtained in a simulation performed for (10,10) CNTs with length  $L_T = 200$  nm and overlap length  $\Delta x_{12} = 40$  nm (b), and a comparison of the temperature distribution in the vicinity of the overlap region with the prediction of an analytical expression derived in Appendix A (c). In panel (a), block arrows indicate the directions of the heat flow. The flux across the overlap regions is created by adding energy at a constant rate  $Q_{HB}$  in the heat bath region in the center of nanotube 1 and removing it from the heat bath region in the center of nanotube 2. Each of the heat bath regions has length of 2 nm. Periodic boundary conditions are applied in the axial direction. The temperature drop at the inter-tube contact,  $\Delta T_{12}$ , is calculated as the difference of the average temperatures of the overlapping CNT segments, as schematically shown in panel (b). In panel (c), the temperature profiles obtained in the MD simulation are shown by black dots and the prediction of Eq. (A4) is shown by thick light curves. The temperature profiles shown in (b) and (c) are obtained by averaging data over 6.7 ns in the steady-state regime.

steady-state regime for an additional period of 4 to 7.7 ns in order to collect data for evaluation of the inter-tube conductance. A representative temperature profile averaged over a period of 6.7 ns in the steady-state regime is shown in Fig. 3(b)

for  $L_T = 200$  nm and  $\Delta x_{12} = 40$  nm. Given that the heat flux through each of the two overlap regions is  $Q_{HB}/2$ , the values of the effective inter-tube conductance per unit overlap length,  $\sigma_T$ , is calculated as  $\sigma_T = Q_{HB}/(2\Delta T_{12}\Delta x_{12})$ , where  $\Delta T_{12}$  is the temperature jump at the CNT-CNT contact defined as the difference of temperatures averaged over the overlap regions in each tube. The calculation of the inter-tube conductance is done by collecting “instantaneous” (averaged over sequential 1 ps windows) values of  $\Delta T_{12}$ , calculating the corresponding instantaneous values of  $\sigma_T$ , and obtaining the average conductance  $\sigma_T$  and the sample standard deviation from the data collected over the steady-state part of the simulation.

To determine the dependence of  $\sigma_T$  on the length of the overlap region, the simulations are performed for  $\Delta x_{12}$  ranging from 10 to 45 nm for  $L_T = 100$  nm and from 10 to 95 nm for  $L_T = 200$  nm. The calculated values of  $\sigma_T$  are shown in Fig. 4 by solid squares and circles for simulations performed for 100 and 200 nm CNTs, respectively. The sample standard deviation is also presented as a measure of uncertainty. All data points are confined within a relatively narrow range from 0.057 to 0.065  $\text{Wm}^{-1}\text{K}^{-1}$ , and are all within one sample standard deviation of each other, thus suggesting that  $\sigma_T$  is independent of the overlap length.

This last conclusion is supported by the comparison of temperature distributions obtained in MD simulations with the ones predicted by an analytical solution of one-dimensional steady-state heat conduction equations for partially overlapping nanotubes, Fig. 3(c). The analytical solution, given in Appendix A, is obtained under assumption of constant values of the intrinsic thermal conductivity of the interacting nanotubes,  $k_T$ , and inter-tube conductance per unit length,  $\sigma_T$ . The inter-tube conductance in the theoretical model is defined by Eq. (A7), which is the same equation that is used in the analysis of the results of atomistic simulations. The theoretical temperature profiles obtained with  $\Delta x_{12}$ ,  $Q_{HB}$ ,  $\Delta T_{12}$ , and  $k_T$  taken from the MD simulation are in very good quantitative agreement with the time-averaged MD temperature distributions (Fig. 3(c)). Small deviations of the MD results from the theoretical curve observed for the right (lower-temperature) CNT can be explained by the temperature dependence of  $k_T$  ( $k_T$  increases and, for fixed heat

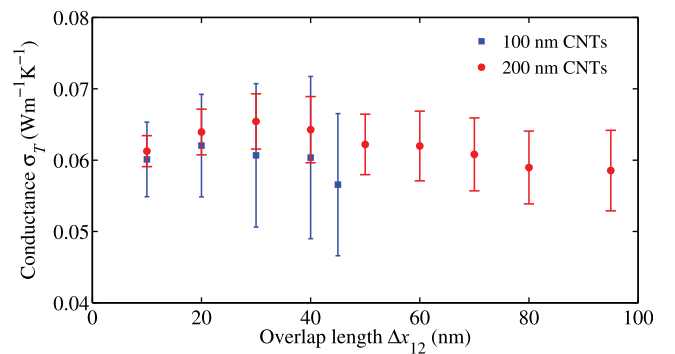


FIG. 4. Inter-tube conductance per unit length,  $\sigma_T$ , versus overlap length,  $\Delta x_{12}$ , obtained in MD simulations of two parallel partially overlapping (10,10) CNTs of 100 nm (blue squares) and 200 nm (red circles) length. The computational setup used in the simulations is shown in Fig. 3(a). The error bars show one sample standard deviation calculated for “instantaneous” values of inter-tube conductance collected during the steady-state part of the simulation.

flux,  $|dT/dx|$  decreases with decreasing  $T$  in the range of temperatures used in the MD simulations<sup>32,55,56</sup>) that is not accounted for in the theoretical model. The good overall agreement between the theoretical model and the results of MD simulations provides an additional support to the assumption of the constant inter-tube conductance per unit length used in the theoretical model.

The values of the inter-tube conductance obtained in this work,  $\sim 0.06 \text{ Wm}^{-1}\text{K}^{-1}$ , are consistent with the results of similar MD simulations reported in Ref. 38 for shorter 25 to 75 nm long (10,10) CNTs, where the conductance of  $0.05\text{--}0.08 \text{ Wm}^{-1}\text{K}^{-1}$  is predicted for overlap lengths ranging from 4 to 9.5 nm. A comparable values of  $0.03 \text{ Wm}^{-1}\text{K}^{-1}$  and  $0.048 \text{ Wm}^{-1}\text{K}^{-1}$  can be calculated from the results of MD simulations performed for two parallel 20 nm long (10,10) CNTs<sup>42</sup> and two parallel 4.3 nm long (10,0) CNTs embedded into a “frozen” matrix,<sup>39,57</sup> respectively. On the other hand, an order of magnitude smaller value of  $0.0048 \text{ Wm}^{-1}\text{K}^{-1}$  can be drawn<sup>58</sup> from the results of MD simulations of non-stationary heat transfer in a bundle of seven (5,5) CNTs reported in Ref. 37. Similarly small values of  $\sigma_T$  can also be calculated from data reported in Ref. 36 for MD simulations performed for 5 to 40 nm long (10,10) CNTs, where the overlap length is varied from 2.5 to 10 nm.

More importantly, the values of inter-tube conductance reported in Ref. 36, when expressed in units of  $\text{Wm}^{-1}\text{K}^{-1}$ , exhibit a strong dependence on the overlap length, e.g.,  $\sigma_T \approx 0.0065 \text{ Wm}^{-1}\text{K}^{-1}$  for 2.5 nm overlap length,  $\sigma_T \approx 0.0034 \text{ Wm}^{-1}\text{K}^{-1}$  for 5 nm overlap length, and  $\sigma_T \approx 0.0018 \text{ Wm}^{-1}\text{K}^{-1}$  for 10 nm overlap length are predicted in simulations performed for 20 and 40 nm long CNTs. This observation of a strong overlap length dependence of  $\sigma_T$  is in sharp contrast with findings of the present study and can be attributed to the small values of  $\Delta x_{12}$  and  $L_T$  considered in Ref. 36. Indeed, a moderate decrease of  $\sigma_T$  with increasing  $\Delta x_{12}$  is also observed in Ref. 38, where the values of  $0.08 \text{ Wm}^{-1}\text{K}^{-1}$  and  $0.05 \text{ Wm}^{-1}\text{K}^{-1}$  can be estimated for (10,10) CNTs from the data shown for 4 and 9.5 nm overlap lengths, respectively. For longer overlap lengths of 10 to 95 nm considered in the present paper, no statistically significant variation of  $\sigma_T$  can be inferred from the results shown in Fig. 4.

The fixed boundary conditions at the ends of the interacting CNTs and the short length of the CNTs used in Ref. 36 could be additional factors responsible for both the strong overlap length dependence of  $\sigma_T$  and the small values of the conductance observed in this work. The dependence on the CNT length is especially pronounced for  $L_T < 10$  nm and is weaker as the length increases from 10 to 40 nm.<sup>36</sup> The observation of the pronounced CNT length dependence for short CNTs is consistent with the results of an MD simulation study of the interfacial conductance between a (5,5) CNT and a surrounding octane liquid,<sup>59</sup> where an increase in the interfacial conductance per CNT surface area with increasing nanotube length is observed up to a length of  $\sim 3.5$  nm and attributed to the extinction of low-frequency phonons in short CNTs. A very weak dependence on the CNT length is reported in Ref. 38 for  $L_T$  ranging from 25 to 75 nm, and no statistically significant difference between the results shown in Fig. 4 for 100 and 200 nm long CNTs is observed.

Overall, the results of the simulations reported in literature and obtained in the present study suggest that the conductance between partially overlapping parallel CNTs is proportional to the length of the overlap (the conductance per length is constant) for conditions relevant to bundles present in real CNT materials, when the CNTs and CNT-CNT overlaps are longer than several tens of nanometers. This conclusion is also consistent with the results of experimental measurements of the thermal conductance between a single walled CNT and a silica substrate, which suggest that the net value of the thermal conductance is proportional to the length of the CNT.<sup>60</sup>

### III. MESOSCOPIC MODEL OF THERMAL CONDUCTIVITY OF BUNDLES OF NANOTUBES

Based on the conclusions of the negligible sensitivity of the intrinsic conductivity of the CNTs to their surroundings in the bundles and the direct proportionality of the inter-tube conductance to the length of the overlap between parallel CNTs, obtained in the MD simulations described above, a robust mesoscopic-level model is developed in this section for analysis of thermal conductivity of CNT bundles. The geometrical model of a bundle is described first, followed by the description of the representation of the thermal transport in CNT bundles, and the dimensional analysis of the average conductivity of bundles.

#### A. Geometrical model of bundles

Both experimental observations<sup>11,12,20</sup> and the results of mesoscopic dynamic simulations<sup>17,19</sup> indicate that individual nanotubes in CNT network materials self-organize into bundles with almost perfect hexagonal packing of CNTs in the bundles, e.g., Fig. 1(b). The analysis reported in the present paper, therefore, is limited to idealized straight bundles of finite thickness with perfect hexagonal ordering of individual CNTs (Fig. 5). The nanotubes in the bundles are arranged along  $N_s$  full shells of axes surrounding a central axis. The total number of axes in a bundle,  $N_a$ , is then defined by  $N_s$  as follows:

$$N_a = 1 + 6 \sum_{n=1}^{N_s} n = 1 + 3(1 + N_s)N_s. \quad (1)$$

The bundle cross-sectional area,  $A_b$ , is defined as a sum of areas of hexagonal Voronoi cells surrounding each axis in the bundle, i.e.,  $A_b = A_a N_a$ , where  $A_a = \sqrt{3}h^2/2$  and  $h$  is the distance between the axes (Fig. 5). Along with such “multi-shell” bundles, an idealized case of a two-axis “bundle,” where individual CNTs are arranged along two parallel axes, is also considered.

Each CNT in a bundle is represented by a straight circular cylinder of constant length  $L_T$ , external radius  $R_T$ , and cross-sectional area  $A_T$  defined in Sec. II A. The ends of neighboring CNTs located on the same axis are separated by a constant axial separation  $\Delta$  (Fig. 6). For a given set of  $N_s$ ,  $L_T$ , and  $\Delta$ , the structure of a bundle is completely defined by positions  $\delta_n$  ( $0 \leq \delta_n < L_T + \Delta$ ,  $n = 1, \dots, N_a$ ) of the right ends of CNTs that either intersect the cross section  $x = 0$  (if  $0 \leq \delta_n < L_T$ ) or are located on the right-hand side of this cross section (if  $L_T \leq \delta_n < L_T + \Delta$ ), see Fig. 6.

Numerical calculations of the heat conduction in bundles are performed for bundles of finite length,  $L_b$ . The total

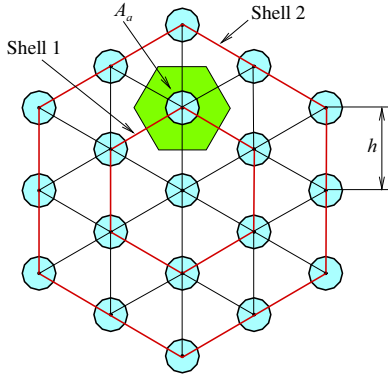


FIG. 5. Example of a cross section of a bundle considered in the mesoscopic model and composed of two shells ( $N_s = 2$ ) around a central CNT axis. Individual CNTs are packed along the hexagonally ordered axes separated from each other by distance  $h$ . The bundle contains  $N_a = 19$  axes as given by Eq. (1). The total number of pairs of nearest neighbor axes in the bundle is  $N_{pair} = 42$  as given by Eq. (3). The area of the bundle cross section is assumed to be equal to  $A_b = N_a A_a$ , where  $A_a$  is the area of the hexagonal Voronoi cell around an internal axis.

number of CNTs in a bundle,  $N$ , is then defined by  $N_s$ ,  $L_b$ ,  $L_T$ , and  $\Delta$ . The CNTs in a finite bundle are indexed by index  $i$  ( $i = 1, \dots, N$ ), where  $x_{i(1)}$ ,  $x_{i(2)}$ , and  $T_i(x)$  denote the coordinates of the left and right ends of CNT  $i$  and one-dimensional temperature distribution along CNT  $i$ , respectively. The implementation of the model for numerical calculation of thermal conductivity does not rely on a particular choice of CNT indexing.

In the theoretical analysis of thermal conductivity of an infinitely long bundle, an indexing from the left to the right is also used for CNTs located on each individual axis. In this case,  $x_{k(1)}^{(n)}$ ,  $x_{k(2)}^{(n)}$ , and  $T_k^{(n)}(x)$  denote the coordinates of the left and right ends and the temperature distribution of the  $k$ th CNT on the  $n$ th axis ( $k = \dots, -2, -1, 0, 1, 2, \dots$ ). On each

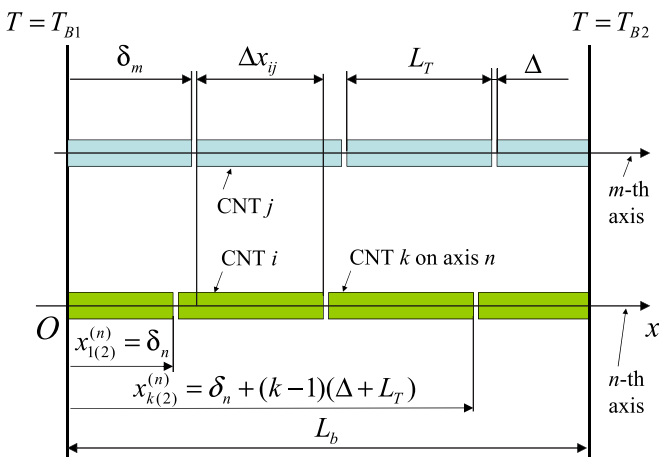


FIG. 6. Schematic representation of an arrangement of CNTs along two neighboring parallel axes,  $n$  and  $m$ , in a CNT bundle. For fixed values of  $L_T$  and  $\Delta$ , the positions of all CNTs on the axes  $n$  and  $m$  are completely defined by the positions of the right ends of the CNT crossing the cross section  $x = 0$ , namely  $\delta_n$  and  $\delta_m$ . Individual nanotubes are identified either by a single index  $i$  (or  $j$ ) or by a pair of subscript  $k$  and superscript  $(n)$ , where  $n$  is the index of an axis and  $k$  is the index of a CNT on this axis. The value of  $\Delta x_{ij}$  is equal to the overlap length for any pair of overlapping neighboring CNTs  $i$  and  $j$  and is equal to 0 for all other pairs of CNTs.

axis  $n$ , the CNT with  $k = 1$  is chosen so that its right end corresponds to  $x_{1(2)}^{(n)} = \delta_n$ .

## B. Thermal transport in bundles

The thermal transport in bundles is governed by the intrinsic conductivity of individual CNTs and the inter-tube thermal conductance in the overlap regions. Only steady-state distributions of temperature in bundles are considered in this work and, therefore, all physical quantities are assumed to be independent of time. The heat conduction in an individual CNT  $i$  is described by the Fourier law,  $Q_i = -k_T A_T dT_i/dx$ , where  $Q_i = Q_i(x)$  is the heat flux through the CNT cross section. In accordance with the results of MD simulations described in Sec. II A, the value of  $k_T$  is assumed to be unaffected by the non-bonding interactions with other CNTs in a bundle and is equal to the axial conductivity of a solitary CNT.

The description of the thermal transport between the neighboring CNTs in a bundle is based on the results of MD simulations reported in Sec. II B, where the conductance through the overlap region between the neighboring CNTs is found to be proportional to the length of the overlap. Namely, the contact conductance for a pair of isothermal CNTs  $i$  and  $j$  lying on neighboring axes and having an overlap region of length  $\Delta x_{ij}$  (Fig. 6) is equal to  $\sigma_T \Delta x_{ij}$  and the corresponding contact heat flux is  $Q_{ij} = \sigma_T \Delta x_{ij} (T_j - T_i)$ . In further derivations, we assume that the value of  $\Delta x_{ij}$  is defined for any pair of CNTs so that  $\Delta x_{ij}$  is equal to the overlap length for pairs of CNTs that are in thermal contact with each other and  $\Delta x_{ij} = 0$  for all other pairs of CNTs. The assumption of isothermal CNTs corresponds to the case of infinitely large intrinsic conductivity of CNTs, which is considered in Sec. IV. For finite intrinsic thermal conductivity, the CNTs are not isothermal. In this case, considered in Sec. V,  $\sigma_T$  is assumed to be independent of the local temperatures of CNTs and, therefore, the heat flux  $Q_{ij}(x)$  between the parts of two neighboring CNTs  $i$  and  $j$  through the part of their overlap region located to the left of coordinate  $x$  can be represented in the form

$$Q_{ij}(x) = \sigma_T \int_{-\infty}^x H_{ij}(\tilde{x}) (T_j(\tilde{x}) - T_i(\tilde{x})) d\tilde{x}, \quad (2)$$

where  $H_{ij}(x)$  is equal to 1 if CNTs  $i$  and  $j$  are located on neighboring axes in the bundle and point  $x$  belongs to their overlap region, otherwise  $H_{ij}(x) = 0$ .

It is worth noting that the assumption of constant values of  $k_T$  and  $\sigma_T$ , used in the present study, can be relaxed if needed for analysis of the effect of the dependence of the heat transfer parameters on geometrical characteristics of the bundle (e.g.,  $N_s$  and  $L_T$ ) and/or temperature. In particular, the dependence of  $k_T$  on  $N_s$ , reported in a number of experimental studies<sup>1,28,29</sup> but not observed in the atomistic simulations discussed in Sec. II A, can be easily accounted for in the model. The computational model can also be straightforwardly generalized for the case when  $k_T$  and  $\sigma_T$  depend on the local CNT temperature. The analytical equations obtained below for the bundle conductivity, however, essentially rely on the independence of  $k_T$  and  $\sigma_T$  on the local CNT temperature.

Two additional assumptions used in the numerical calculations and theoretical analysis reported in the present paper are the ones that the bundles are longer than individual CNTs ( $L_b > L_T$ ) and the contact heat transfer between neighboring CNTs lying on the same axis is negligible. Thus, the non-zero thermal conductivity of a bundle is the result of contact heat transfer between overlapping CNTs lying on neighboring axes. Each CNT from an internal shell can interact with CNTs located on six neighboring axes, while a CNT from the external shell has neighbors lying on four or three axes. Among all possible random distributions of CNTs in a bundle, there are distributions that correspond to non-percolating bundles with zero conductivity. In a non-percolating bundle, the condition  $|\delta_n - \delta_m| \leq \Delta$  is satisfied for any pair of the neighboring axes  $n$  and  $m$ .

In numerical calculations, the temperature gradient  $\nabla T_x = dT/dx$  of the averaged temperature  $T(x)$  along a bundle of finite length  $L_b$  is maintained by fixing temperatures  $T_{B1}$  and  $T_{B2}$  at the left (at  $x = 0$ ) and right (at  $x = L_b$ ) ends of the bundle. In order to characterize the position of CNT  $i$  with respect to the boundaries, a variable  $\chi_i$  is introduced, which is equal to 1 if CNT  $i$  intersects the left boundary, equal to 2 if the CNT intersects the right boundary, and equal to 0 otherwise. The temperature of CNT  $i$  with  $\chi_i \neq 0$  at a point where it intersects the plane  $x = 0$  or  $x = L_b$  is assumed to be equal to the temperature  $T_{B1}$  or  $T_{B2}$ , correspondingly. As described below,  $\nabla T_x \neq \nabla T_{Bx} = (T_{B2} - T_{B1})/L_b$  and  $\nabla T_x$  should be calculated in the course of the calculations based on the temperatures of individual CNTs. In the theoretical consideration of infinitely long bundles, the temperature gradient  $\nabla T_x$  is an imposed parameter of the problem.

The goal of the analysis reported in Secs. IV and V is to evaluate the ensemble-averaged values of thermal conductivity for bundles at fixed values of  $L_T$ ,  $\Delta$ , and  $N_s$  (and  $L_b$  for finite-length bundles considered in numerical calculations), assuming that parameters  $\delta_n$ , characterizing the structure of an individual bundle, are independent random variables ranging from 0 to  $L_T + \Delta$ .

The ensemble-averaged heat flux through any cross section of the bundle that is perpendicular to its axis  $Ox$  is assumed to be described by the Fourier law  $\langle Q \rangle = -k_b A_b \nabla T_x$ , where  $k_b$  is the averaged axial thermal conductivity of the bundle and brackets  $\langle \dots \rangle$  denote averaging over all possible values of  $\delta_n$ . The flux  $\langle Q \rangle$  can be represented as  $\langle Q \rangle = N_{pair} \langle Q_{pair} \rangle$ , where  $\langle Q_{pair} \rangle$  is the contribution to the averaged heat flux provided by any pair of neighboring axes in the bundle and  $N_{pair}$  is the total number of pairs of neighboring axes in the bundle

$$N_{pair} = 6 \sum_{n=1}^{N_s} (2 + 3(n-1)) = 3N_s(3N_s + 1). \quad (3)$$

In general,  $\langle Q_{pair} \rangle$  may depend on the thickness of the bundle, i.e., on  $N_s$  or  $N_{pair}$ ; although in certain cases, this dependence is weak and can be neglected. The thermal conductivity  $k_b$  can be represented as follows:

$$k_b = -\frac{N_{pair} \langle Q_{pair} \rangle}{N_a A_a \nabla T_x}. \quad (4)$$

### C. Dimensional analysis of the averaged conductivity of bundles

In order to define  $k_b$  based on Eq. (4), one needs to calculate  $\langle Q_{pair} \rangle$  for a given set of parameters  $N_s$ ,  $L_T$ ,  $\Delta$ ,  $\sigma_T$ , and  $k_T A_T$ , and for an imposed temperature gradient  $\nabla T_x$ . The value of  $A_a$  does not affect the temperature distribution. The results of numerical calculations are also assumed to be independent of  $L_b$  if  $L_b$  is sufficiently large. Thus,  $\langle Q_{pair} \rangle$  depends on six governing parameters including five dimensional parameters and  $N_s$ .

In order to reduce the number of independent governing parameters in scaling laws for the conductivity of bundles, one can introduce reduced variables, which are further denoted by the bar over the variable as compared to corresponding dimensional variables having no bar. In particular, any dimensionless length variables, e.g., coordinates  $\bar{x}$ , are introduced based on the length scale  $L_T$ , any temperature variables, e.g., CNT temperature  $\bar{T}_i$ , are introduced based on the temperature scale  $\nabla T_x L_T$ , and the dimensionless thermal conductivity of a bundle  $\bar{k}_b$  is introduced based on the scale  $k_* = \sigma_T L_T^2 / A_a$ , i.e.,  $\bar{x} = x/L_T$ ,  $\bar{T}_i = T_i / (\nabla T_x L_T)$ , and  $\bar{k}_b = k_b / k_*$ . For the five dimensional governing parameters and three independent units, e.g., m, W, and K in SI, Buckingham's  $\Pi$ -theorem, e.g., Ref. 61, allows one to conclude that any dimensionless parameter of the system then depends only on two independent dimensionless governing parameters and, additionally, on  $N_s$ . These governing parameters can be chosen, e.g., in the form of the reduced axial spacing  $\bar{\Delta} = \Delta / L_T$  and the Biot number  $\text{Bi} = \sigma_T L_T^2 / (k_T A_T)$ , which characterizes the role of the contact heat transfer with respect to the intrinsic heat conduction in individual CNTs. Equation (4) for the averaged thermal conductivity can then be rewritten in reduced units as

$$\bar{k}_b = -\frac{N_{pair}(N_s)}{N_a(N_s)} \langle \bar{Q}_{pair} \rangle (N_s, \text{Bi}, \bar{\Delta}), \quad (5)$$

where  $\langle \bar{Q}_{pair} \rangle = \langle Q_{pair} \rangle / (\sigma_T L_T^2 \nabla T_x)$ .

In Secs. IV and V, the dependence of  $\bar{k}_b$  on  $N_s$ ,  $\bar{\Delta}$ , and Bi is established theoretically and verified in numerical calculations. For systems where the conductivity is dominated by the thermal contact conductance and the intrinsic conductivity is relatively large, the Biot number is small, and temperature gradients along individual CNTs are small.<sup>62</sup> In the limit of  $\text{Bi} \rightarrow 0$ , the temperature gradients along nanotubes vanish and the CNTs become isothermal. This limiting case is considered next, in Sec. IV.

## IV. BUNDLES OF NANOTUBES WITH INFINITELY LARGE INTRINSIC CONDUCTIVITY

### A. Computational model

In the case of infinitely large intrinsic thermal conductivity of individual CNTs ( $\text{Bi} = 0$ ), each CNT has a constant temperature  $T_i$ . Consequently, the nanotubes crossing the boundaries have temperatures equal to either  $T_{B1}$  or  $T_{B2}$ . In the steady state, the temperature of an internal CNT ( $\chi_i = 0$ ) can be found by balancing all contact heat fluxes through the overlap regions between this CNT and all other CNTs, i.e.,

$\sum_{j=1}^N Q_{ij} = 0$ , where  $Q_{ij} = \sigma_T \Delta x_{ij} (T_j - T_i)$ . Hence, the temperatures of all CNTs in a finite-length bundle can be found by solving the following system of linear equations:

$$\sum_{j=1}^N \Delta x_{ij} (T_j - T_i) = 0 \quad \text{if } \chi_i = 0 \quad (\text{i.e., for all internal CNTs}), \quad (6a)$$

$$T_i = T_{B\chi_i} \quad \text{if } \chi_i = 1, 2 \quad (\text{i.e., for CNTs at the ends of the bundle}). \quad (6b)$$

The heat flux through the cross section at  $x = 0$  can be calculated as

$$Q_{B1} = -\sigma_T \sum_{i=1, \chi_i=1}^N \sum_{j=1}^N \Delta x_{ij} (T_j - T_i), \quad (7)$$

and a similar equation can be written for the heat flux  $Q_{B2}$  through the cross section at  $x = L_b$ . In the steady state,  $Q = Q_{B1} = Q_{B2}$  and any bundle cross section can be used for calculation of  $Q$ . Then,  $\langle \bar{Q}_{pair} \rangle$  can be found, e.g., using the following equation:

$$\langle \bar{Q}_{pair} \rangle = -\frac{1}{N_{pair}} \left\langle \sum_{i=1, \chi_i=1}^N \sum_{j=1}^N \Delta \bar{x}_{ij} (\bar{T}_j - \bar{T}_i) \right\rangle. \quad (8)$$

The numerical procedure used in the calculations is as follows. Equations (6) are first solved iteratively by the Gauss-Seidel method,<sup>63</sup> until the condition  $|Q_{B1} - Q_{B2}| < (1/2)(Q_{B1} + Q_{B2})\Delta_Q$  is satisfied with tolerance  $\Delta_Q = 10^{-7}$ . In order to calculate  $T(x)$  and find  $\nabla T_x$ , a bundle is divided into a one-dimensional mesh of cells with size  $\Delta x$  in the direction of the  $x$ -axis. The value of  $T(x)$  within a cell is calculated by averaging temperatures of all CNTs that are crossing this cell, with contributions to the averaging from CNTs ending within the cell weighted according to the parts of their lengths that belong to the cell. The procedure of evaluation of  $T(x)$  is repeated for a sufficiently large (from  $2 \times 10^4$  to  $10^5$ ) number of bundles with different sets of random values  $\delta_n$  in order to ensure that statistical error of the ensemble-averaging is within 0.1% of the values evaluated in the calculations.

An example of an ensemble-averaged temperature profile is shown in Fig. 7 for  $N_s = 1$ ,  $\Delta = 0$ , and  $L_b/L_T = 4$ . In all bundles with  $L_b > 2L_T$  and  $Bi = 0$  (e.g., the solid curve in Fig. 7), the distribution  $T(x)$  consists of a central part, where the distribution is truly linear and the temperature gradient is constant and somewhat larger than  $\nabla T_{Bx} = (T_{B2} - T_{B1})/L_b$ , and boundary regions where the absolute value of the temperature gradient decreases in the vicinity of the boundaries. These boundary regions with non-linear distributions of  $T(x)$  have widths of  $\Delta L = L_T$  and correspond to the regions where CNTs linked to the boundaries are present. The boundary regions are excluded from the calculation of the temperature gradient, i.e.,  $\nabla T_x$  is determined based on the linear part of  $T(x)$  in the central region of the bundle,  $\Delta L \leq x \leq L_b - \Delta L$ . Although the temperature gradient in the central part of the bundle becomes practically independent

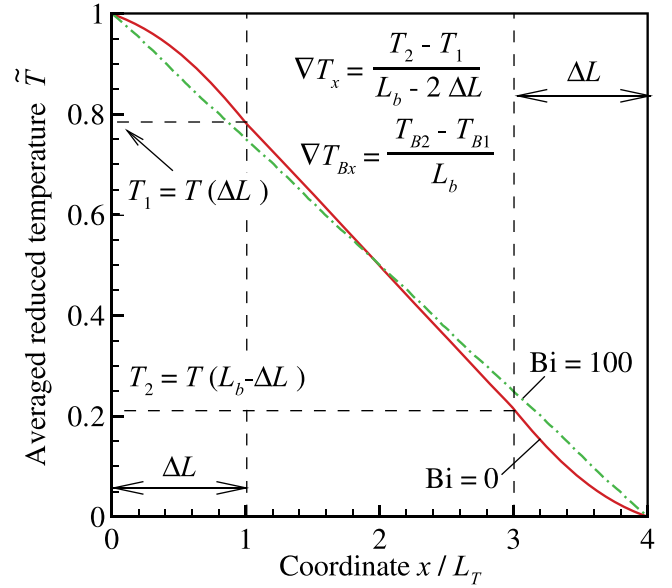


FIG. 7. Distribution of the ensemble-averaged reduced temperature  $\bar{T} = (T - T_{B2})/(T_{B1} - T_{B2})$  along the bundle length  $x/L_T$ , obtained in numerical calculations at  $N_s = 1$ ,  $\Delta = 0$ , and  $L_b/L_T = 4$  for  $Bi = 0$  (solid curve) and  $Bi = 100$  (dashed-dotted curve). The temperature gradient,  $\nabla T_x = (T(L_b - \Delta L) - T(\Delta L))/(L_b - 2\Delta L)$ , is calculated based on the central part of the temperature profile,  $\Delta L < x < L_b - \Delta L$ , as shown in the figure. At  $Bi = 0$ , the value of  $\nabla T_x$  is different from  $\nabla T_{Bx} = (T_{B2} - T_{B1})/L_b$  due to the non-linear distribution of temperature in the vicinity of boundaries.

of  $L_b/L_T$  for  $L_b/L_T > 3$ , all results at  $Bi = 0$  are obtained with  $L_b/L_T = 32$  in order to ensure faster convergence of the ensemble averaging. In the calculations performed with  $\Delta > 0$ , when the formation of non-percolating bundles is possible, the distributions  $T(x)$  and values of  $\nabla T_x$  are determined by averaging results obtained only for percolating bundles with  $Q \neq 0$ . Finally, once  $\nabla T_x$  is found, the ensemble-averaged values of  $\langle \bar{Q}_{pair} \rangle$  and  $\bar{k}_b$  are calculated with Eqs. (8) and (5), respectively.

## B. Theoretical analysis of thermal conductivity

The theoretical evaluation of the averaged thermal conductivity  $k_b^0$  for  $Bi = 0$  is based on the assumption that, to the first approximation, the contribution of the conduction between CNTs lying on a pair of neighboring axes in a bundle does not depend on the conduction between CNTs lying on any other pair of axes. In order to calculate  $\langle Q_{pair} \rangle$ , one then needs to consider the temperature distribution in a two-axis bundle (Fig. 6).

The analysis of bundle conductivity can be limited to bundles with  $\Delta < L_T$ , because at  $\Delta \geq L_T$ , the two-axis bundle does not conduct heat. The relative positions of CNTs in the two-axis bundle is characterized by a single parameter  $\delta = \delta_1 - \delta_2$  that varies from  $-(L_T + \Delta)$  to  $L_T + \Delta$ . We first consider only percolating bundles with  $|\delta| > \Delta$  and then account for the contribution of non-percolating bundles with  $|\delta| \leq \Delta$ . For the sake of convenience, only the case when  $\delta > 0$  will be considered, because the opposing case when  $\delta < 0$  is completely symmetrical and can be obtained from the former by changing the indexes of the axes. The

temperatures of individual CNTs should then satisfy Eq. (6a) that, in the case of the two-axis bundle, reduces to

$$\Delta x_2(T_k^{(2)} - T_k^{(1)}) + \Delta x_1(T_{k+1}^{(2)} - T_k^{(1)}) = 0 \quad \text{for CNTs on axis 1,} \quad (9a)$$

$$\Delta x_1(T_{k-1}^{(1)} - T_k^{(2)}) + \Delta x_2(T_k^{(1)} - T_k^{(2)}) = 0 \quad \text{for CNTs on axis 2,} \quad (9b)$$

where  $\Delta x_1 = \delta - \Delta$  and  $\Delta x_2 = L_T - \Delta - \Delta x_1$  are the corresponding overlaps. The solution of Eqs. (9) has a form

$$T_k^{(2)} = T_{k-1}^{(1)} + (1 - \alpha)\Delta T, \quad T_k^{(1)} = T_k^{(2)} + \alpha\Delta T, \quad (10)$$

where  $\alpha = \Delta x_1/(L_T - \Delta)$  and  $\Delta T = \nabla T_x(L_T + \Delta)$  is the temperature difference between a pair of neighbor CNTs lying on the same axis. The solution given by Eq. (10) is not unique. A unique solution for the temperature distribution can be obtained by fixing the temperature of a single CNT in the bundle, e.g.,  $T_1^{(1)} = T_0$ , where  $T_0$  is the imposed temperature of nanotube 1 on axis 1.

The heat flux through the bundle can be found with Eq. (8) that reduces to

$$\begin{aligned} \langle \bar{Q}_{pair} \rangle_p &= -\langle \Delta \bar{x}_1 (\bar{T}_2^{(2)} - \bar{T}_1^{(1)}) \rangle = -(1 - \bar{\Delta}^2) \langle \alpha(1 - \alpha) \rangle \\ &= -\frac{1}{6}(1 - \bar{\Delta}^2), \end{aligned} \quad (11)$$

where the subscript “ $p$ ” indicates that Eq. (11) accounts for the contribution of percolating bundles only, and  $\langle \alpha(1 - \alpha) \rangle$  is calculated as  $\langle \alpha(1 - \alpha) \rangle = \int_0^1 \bar{x}(1 - \bar{x})d\bar{x} = 1/6$  assuming that  $\alpha$  is distributed with equal probability between 0 and 1 (the case of  $\alpha < 0$  implies  $\delta \leq \Delta$  and corresponds to a non-percolating bundle). Since the percolation probability is equal to

$$P_p = 1 - P(|\delta| \leq \Delta) = (1 - \bar{\Delta}^2)/(1 + \bar{\Delta})^2, \quad (12)$$

the ensemble-averaged value of the heat flux for all possible bundles is defined as  $\langle \bar{Q}_{pair} \rangle = \langle \bar{Q}_{pair} \rangle_p P_p = -(1 - \bar{\Delta})^2/6$ . By inserting this equation into Eq. (5), the averaged thermal conductivity of a bundle with  $N_s$  shells can be written in the following form

$$\bar{k}_b^0 = \frac{1}{12} f^0(N_s) g(\bar{\Delta}), \quad (13)$$

where the “thickness” function

$$f^0(N_s) = \frac{2N_{pair}}{N_a} = 6 \frac{3N_s^2 + N_s}{3N_s^2 + 3N_s + 1}, \quad (14)$$

and the “density” function

$$g(\bar{\Delta}) = [H(1 - \bar{\Delta})]^2 \quad (15)$$

account for the number of shells in the bundle and the axial separation within the bundle. The Heaviside step function,  $H(x)$  ( $H(x) = x$  for  $x > 0$  and  $H(x) = 0$  otherwise), is used

in Eq. (15) in order to extend Eq. (13) to the case where  $\bar{\Delta} \geq 1$ , when any two-axis bundle is non-percolating and  $k_b^0 = 0$ . The thickness function,  $f^0(N_s)$ , is equal to the ratio of the conductivity of a bundle with  $N_s$  shells to the conductivity of the two-axis bundle. In the limit of an infinitely thick bundle,  $N_s \rightarrow \infty$ ,  $f^0(N_s) \rightarrow 6$ , and Eq. (13) reduces to  $\bar{k}_b^0 = g(\bar{\Delta})/2$ . Another limiting case, further referred to as a case of  $N_s = 0$ , is a bundle composed of two axes only. The conductivity of the two-axis bundle is  $\bar{k}_b^0 = g(\bar{\Delta})/12$ , since  $N_{pair} = 1$ ,  $N_a = 2$ , and  $f^0 = 2N_{pair}/N_a = 1$  for such bundle. In order to apply Eq. (13) to the two-axis bundle, the thickness function at  $N_s = 0$  should be defined as  $f^0(0) = 1$ .

In the case when  $\Delta = 0$ , Eq. (13) predicts that  $k_b^0 \propto L_T^2$ . The reason for this result is obvious from Eq. (11): The change in the CNT length results in the proportional changes of both the averaged overlap between a pair of CNTs,  $\langle \Delta x_1 \rangle$ , and the averaged temperature difference,  $\langle T_2^{(2)} - T_1^{(1)} \rangle$ . As a result, the heat flux  $\langle Q_{pair} \rangle$  is a quadratic function of  $L_T$ . The derivation of Eq. (13) shows that an increase in  $\Delta$  decreases the averaged thermal conductivity, because it decreases the heat flux in percolating bundles and increases the probability of the formation of non-percolating bundles. In the case where  $\bar{\Delta} \geq 1$ , any two-axis bundle is non-percolating, while percolation is still possible in bundles composed of more than two axes. For instance, a bundle with  $N_s = 1$  (seven axes) can have non-zero conductivity at  $\bar{\Delta} = 1$  (e.g., if  $\delta_n = nL_T/6$  and axes are indexed in the order of rotation around the central axis, which has  $n=0$ ). Thus, Eq. (13) with the density function given by Eq. (15) provides a good approximation of the conductivity at sufficiently small  $\bar{\Delta}$ ; whereas for larger axial separations, the heat transfer between different pairs of axes is not independent from each other. The accuracy of Eqs. (13)–(15) is further evaluated below by comparing the theoretical predictions with solutions of the numerical model described in Sec. IV A.

### C. Comparison of the theoretical model with numerical results

In order to evaluate the accuracy of the theoretical equations derived above, a series of numerical calculations of the bundle conductivity is performed for  $Bi = 0$ ,  $1 \leq N_s \leq 8$ , and  $0 \leq \bar{\Delta} \leq 1$ . Two-axis bundles ( $N_s = 0$ ) are also considered.

At  $\Delta = 0$ , the numerical values of conductivity per number of axis pairs in the bundle,  $\bar{k}_b^0/f^0(N_s)$ , are found to be independent of the number of shells,  $N_s$ , and coincide with the theoretical value  $1/12$  predicted by Eq. (13) within the computational error (Fig. 8(a)). This result shows that the hypothesis on the statistically independent nature of the heat conduction in different pairs of neighboring CNTs is valid at  $\Delta = 0$ .

At  $\Delta > 0$ , the values of  $\bar{k}_b^0/f^0(N_s)$  exhibit substantial increase with increasing  $N_s$  for thin bundles (Fig. 8(a)) but rapidly saturate and become practically independent of  $N_s$  at  $N_s \geq 4$ . In particular, the thickness function  $f^0(N_s)$  given by Eq. (14) is equal to  $\sim 5.11$  at  $N_s = 4$ , which is only  $\sim 15\%$  below the limiting value of 6 at  $N_s \rightarrow \infty$ . This rapid saturation is related to the decreasing ratio of the number of CNTs

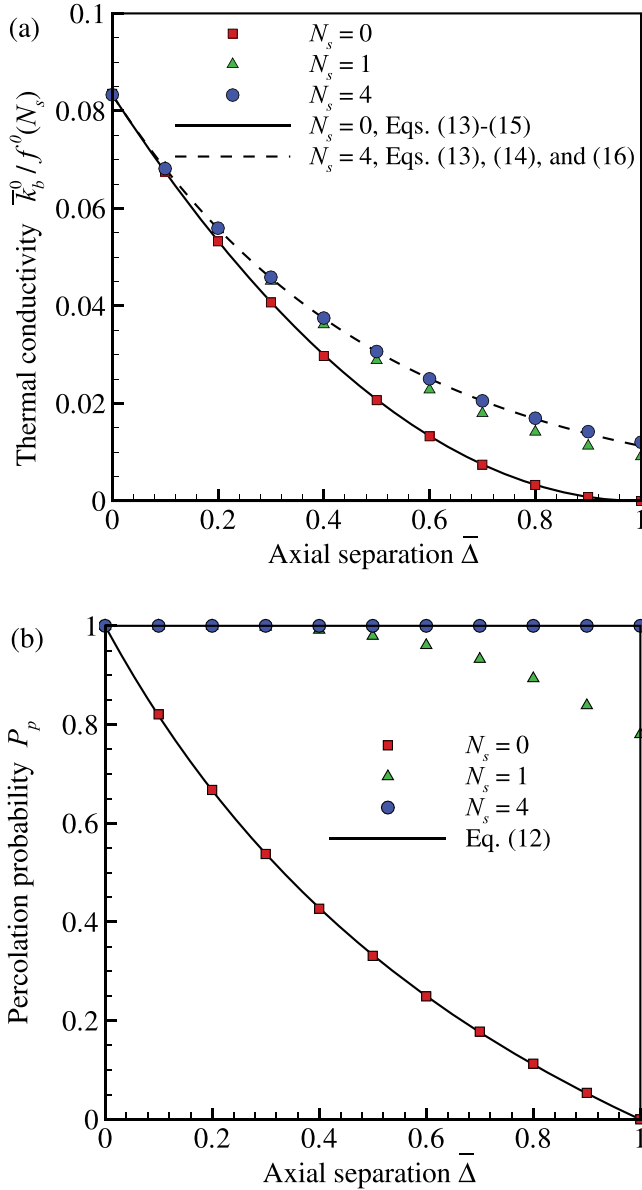


FIG. 8. The dependences of the dimensionless thermal conductivity of a bundle at  $\text{Bi} = 0$  scaled by the thickness function,  $\bar{k}_b^0/f^0(N_s)$  (a) and percolation probability  $P_p$  (b) on the axial separation,  $\Delta/L_T$ , calculated for different  $N_s$ . The symbols represent values obtained numerically and lines show the theoretical predictions. In panel a, the solid curve for  $N_s = 0$  is obtained with Eqs. (13)–(15) and the dashed curve is obtained with Eqs. (13), (14), and (16). In panel b, the solid curve is obtained for  $N_s = 0$  with Eq. (12).

on the bundle external shell to the total number of CNTs in the bundle.

The dependence of  $\bar{k}_b^0$  on  $\bar{\Delta}$ , predicted by Eqs. (13)–(15) (solid curve in Fig. 8(a)), coincides with the numerical results for  $N_s = 0$ . For thick bundles ( $N_s \gg 1$ ), however, the predictions of the theoretical equations are in fairly good agreement with numerical results only for small  $\bar{\Delta}$ , in the range  $0 \leq \bar{\Delta} \leq 0.1$ . At larger  $\bar{\Delta}$ , the results of the numerical calculations deviate from the predictions of Eqs. (13)–(15), with the theoretical predictions underestimating the values obtained in the calculations. This deviation is the result of “chain” interactions, where the percolation probability  $P_p$  becomes much larger than that given by Eq. (12) for the two-axis bundle. Indeed, while numerical values of  $P_p$  coincide

with the curve obtained with Eq. (12) for  $N_s = 0$ , the percolation probability remains very close to unity for  $N_s \geq 4$  at  $\bar{\Delta} \leq 1$  (Fig. 8(b)).

It is worth noting, however, that consideration of very large separations for bundles composed of high-aspect ratio nanotubes within the present model may be meaningless, since at  $\Delta \gg R_T$ , the van der Waals attraction between CNTs in a bundle can bend the nanotubes so that they fill the gaps and reduce the inter-tube interaction energy. The ideal geometry of the bundle adopted in the present model will no longer be valid in this case. In real CNT materials, the ratio  $R_T/L_T$  is usually smaller than  $10^{-2}$  and can be as small as  $10^{-3}$ – $10^{-4}$ ,<sup>64</sup> so that the condition  $\bar{\Delta} < 0.1$  corresponds to  $\Delta < (10 - 10^3)R_T$ . Thus, the theoretical model of the bundle conductivity with the density function given by Eq. (15) is valid up to quite large separations when measured in CNT radii.

In the present model, the inverse axial separation  $1/\bar{\Delta}$  plays the role of a density parameter that controls the density of the material and transition to percolation. It was found in Ref. 65 for two-dimensional fibrous materials that the factor describing the effect of correlation between temperatures of individual fibers on the thermal conductivity of the CNT material can be accurately expressed in terms of an exponential function of the inverse density parameter. Here, we apply the same idea in order to find a semi-empirical density function  $g(\bar{\Delta})$  that replaces Eq. (15) for thick bundles with  $N_s \geq 4$ . Namely, one can represent this function in the form  $g(\bar{\Delta}) = \exp(-\mu\bar{\Delta})$ , where the constant  $\mu$  can be found from the condition that the last equation and Eq. (15) have the same derivatives at  $\Delta = 0$ . This condition yields  $\mu = 2$ , and the semi-empirical equation for the density function at large  $N_s$  can be written in the form

$$g(\bar{\Delta}) = \exp(-2\bar{\Delta}). \quad (16)$$

Using  $g(\bar{\Delta})$  given by Eq. (16) in Eq. (13), we obtain an accurate approximation of  $\bar{k}^0$  for thick bundles ( $N_s \geq 4$ ) in the range  $\bar{\Delta} \leq 1$ , e.g., dashed curve in Fig. 8(a).

## V. BUNDLES OF NANOTUBES WITH FINITE INTRINSIC CONDUCTIVITY

### A. Computational model

In the case of finite intrinsic conductivity of CNTs ( $\text{Bi} > 0$ ), the nanotubes are not isothermal and the heat exchange between the nanotubes is defined by the distribution of temperatures along the nanotubes that are in contact with each other. The steady-state temperature distribution in nanotube  $i$ ,  $T_i(x)$ , can be found by solving a system of one-dimensional steady-state heat conduction equations with source terms that account for the contact heat transfer

$$A_T k_T \frac{d^2 T_i}{dx^2} = - \sum_{j=1, j \neq i}^N q_{ij}(x), \quad (17)$$

where  $q_{ij}(x) = dQ_{ij}(x)/dx = \sigma_T H_{ij}(x)(T_j(x) - T_i(x))$  is the linear density of contact heat flux between CNTs  $i$  and  $j$ . In order to obtain a unique solution of Eqs. (17) for all CNTs in

a bundle, we use the boundary conditions that impose fixed temperatures of  $T_{B1}$  and  $T_{B2}$  at  $x = 0$  and  $x = L_b$  for CNTs that cross the bundle cross sections at these locations that are considered as two ends of the bundle, while at any end of a CNT positioned between 0 and  $L_b$ , the heat flux is set to be equal to zero, i.e.,

$$T_i(0) = T_{B\chi_i} \quad \text{if } \chi_i = 1, \quad (18a)$$

$$\frac{dT_i}{dx}(x_{i(k)}) = 0 \quad \text{if } 0 < x_{i(k)} < L_b, \quad (18b)$$

$$T_i(L_x) = T_{B2} \quad \text{if } \chi_i = 2. \quad (18c)$$

In order to solve Eqs. (17) and (18) numerically, a one-dimensional mesh is introduced that discretizes the bundle along the axis  $Ox$  into  $M$  cells of length  $\Delta x = L_b/M$  with coordinates of the cell boundaries,  $x_m = m\Delta x$  ( $m = 0, \dots, M$ , Fig. 9). The temperature distribution along CNT  $i$  can then be represented by a set of discrete values of temperature  $T_{i,m}$  at points  $x_m$ , where  $m$  varies from  $J_{i(1)}$  to  $J_{i(2)}$  that correspond to the smallest interval of mesh nodes ( $x_{J_{i(1)}}, x_{J_{i(2)}}$ ) containing the whole CNT. This method of “global” discretization of the bundle allows one to obtain a conservative numerical scheme that ensures conservation of energy in the system and results in the following equation for the temperature at any internal node of the CNT:

$$T_{i,m+1} - 2T_{i,m} + T_{i,m-1} = \text{Bi}\Delta\bar{x} \sum_{j=1, j \neq i}^N \Delta\bar{x}_{ij,m} (T_{i,m} - T_{j,m}), \quad (19)$$

if  $m = J_{i(1)} + 1, \dots, J_{i(2)} - 1$ ,

where  $\Delta\bar{x}_{ij,m}$  is the dimensionless length of the overlap between CNTs  $i$  and  $j$  belonging to the interval  $(x_m - \Delta x/2, x_m + \Delta x/2)$ . Definition of  $\Delta\bar{x}_{ij,m}$  implies that  $\Delta\bar{x}_{ij,m} = \Delta\bar{x}_{ji,m}$  for any  $i, j$ , and  $m$ . In order to maintain a constant heat flux through any cross section of the bundle,  $\Delta\bar{x}_{ij,m}$  is set to zero if  $m$  corresponds to one of the ends of CNTs  $i$

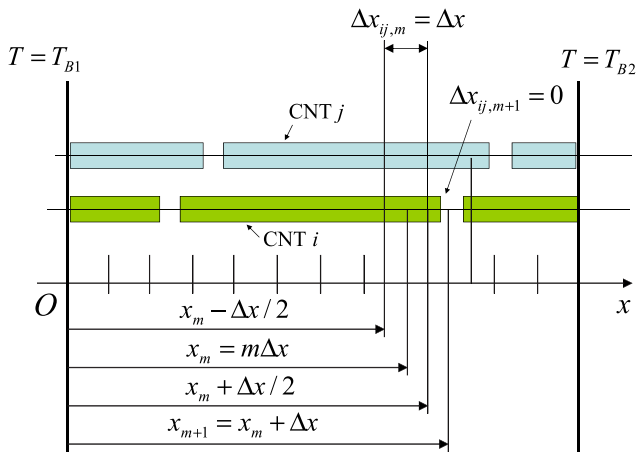


FIG. 9. Schematic representation of the spatial discretization used in the numerical calculation of CNT temperatures in the case  $\text{Bi} > 0$ . The bundle is discretized into cells of length  $\Delta x$ , with cell boundaries given by coordinates  $x_m$ . The overlap length between CNTs  $i$  and  $j$  within cell  $m$ ,  $\Delta x_{ij,m}$ , is equal to  $\Delta x$  if the cell is fully covered by the overlap region, otherwise  $\Delta x_{ij,m} = 0$ .

or  $j$ , i.e.,  $\Delta\bar{x}_{ij,m} = 0$  if  $m = J_{i(k)}$  or  $m = J_{j(k)}$ ,  $k = 1, 2$ . The temperature in the first ( $m = J_{i(1)}$ ) or last ( $m = J_{i(2)}$ ) mesh nodes of CNT  $i$  is assumed to be equal to the corresponding heat bath temperature in accordance with Eqs. (18a) and (18c) if the CNT crosses the left or right boundary of the bundle. If a CNT end is positioned inside the bundle, the temperature of the corresponding first or last nodes of the CNT is set to be equal to the temperature of the nearest internal node of the same CNT in order to implement the zero flux condition given by Eq. (18b).

When Eq. (19) is solved and distributions of temperature along CNTs are found, the heat flux  $Q$  through the system can be calculated for the cross section at  $x = 0$  in the form

$$Q_{B1} = -\sigma_T \sum_{i=1, \chi_i=1}^N \sum_{j=1}^N \sum_{m=1}^{M-1} \Delta x_{ij,m} (T_{j,m} - T_{i,m}), \quad (20)$$

and a similar equation can be written for the heat flux  $Q_{B2}$  through the cross section at  $x = L_b$ . Since the numerical scheme implies precise energy conservation, the condition  $Q_{B1} = Q_{B2}$  is valid for any solution of Eq. (19) and  $\langle \bar{Q}_{pair} \rangle$  can be found, e.g., in the form

$$\langle \bar{Q}_{pair} \rangle = -\frac{1}{N_{pair}} \left\langle \sum_{i=1, \chi_i=1}^N \sum_{j=1}^N \sum_{m=1}^{M-1} \Delta\bar{x}_{ij,m} (\bar{T}_{j,m} - \bar{T}_{i,m}) \right\rangle \quad (21)$$

that is similar to Eq. (8). The important difference between Eqs. (8) and (21), however, is that the latter predicts more complex dependence of  $\langle \bar{Q}_{pair} \rangle$  on  $L_T$ , which is defined by dependence of the reduced temperatures in the right-hand part of Eq. (21) on  $\text{Bi}$  that varies with  $L_T$ . The set of Eqs. (19) is solved iteratively by the Gauss-Seidel method, with iterations performed until the condition  $|Q_{B1} - Q_{B2}| < (1/2)(Q_{B1} + Q_{B2})\Delta_Q$  is satisfied. Numerical error introduced due to the “global” discretization of bundles is briefly discussed in Sec. VC.

## B. Theoretical analysis of thermal conductivity

In this section, we perform a theoretical analysis of the average conductivity of bundles composed of CNTs with finite intrinsic thermal conductivity, i.e., at  $\text{Bi} > 0$ . For simplicity, the analysis is limited to the case of  $\Delta = 0$ , when the heat transfer in a bundle with arbitrary  $N_s$  can be reduced to the heat transfer in a two-axis bundle. A simplified approach aimed at establishing the approximate scaling dependence of  $k_b$  on the geometrical and heat transfer parameters of the bundle is applied first and is followed by a more accurate solution.

For a two-axis bundle with  $\Delta = 0$ , the relative position of two overlapping CNTs lying on different axes is completely determined by a single geometrical parameter  $\delta = \delta_2 - \delta_1$ . Following an approach developed in Ref. 49 for calculation of thermal conductivity of a system of dispersed, randomly distributed nanotubes, one can assume that distribution of temperature,  $T_i(x)$ , along any CNT  $i$  is close to a linear one and can be represented in the form

$$T_i(x) = T_0 + \nabla T_x x_{C_i} + \left\langle \frac{dT_i}{dx} \right\rangle (x - x_{C_i}), \quad (22)$$

where  $x_{C_i}$  is the coordinate of the center of CNT  $i$ ,  $T_0$  is the predefined temperature of the bundle at  $x=0$ , and  $\langle dT_i/dx \rangle = \langle (T_i(x_{i(2)}) - T_i(x_{i(1)}))/L_T \rangle$  is the ensemble-averaged gradient of temperature in the CNT averaged over the length of the CNT. Equation (22) allows one to express the temperature difference in the right part of Eq. (17) as

$$T_j(x) - T_i(x) = \left( \nabla T_x - \left\langle \frac{dT_i}{dx} \right\rangle \right) \Delta x_{C_{ij}}, \quad (23)$$

where  $\Delta x_{C_{ij}} = x_{C_j} - x_{C_i}$ . Then, one can integrate Eq. (17), e.g., for CNT 1 on axis 1 and find a relation between  $\nabla T_x$  and  $\langle dT_i/dx \rangle$ . For the sake of simplicity, we assign new indexes 0, 1, and 2 for three CNTs to be considered, so that the temperature of CNT 1 on axis 1 is  $T_1 = T_1^{(1)}$  and the temperatures of CNTs 0 and 2 on axis 2 are  $T_0 = T_1^{(2)}$  and  $T_2 = T_2^{(2)}$ . Then, one can find that

$$\frac{T_1(\delta) - T_1(0)}{L_T} = -\frac{\sigma_T}{A_T k_T L_T} F_{10}(\delta), \quad (24a)$$

$$\frac{T_1(L_T) - T_1(\delta)}{L_T} = \frac{\sigma_T}{A_T k_T L_T} F_{12}(\delta), \quad (24b)$$

where the right-hand parts can be calculated using the temperature difference written in the form of Eq. (23) as follows:

$$F_{10}(\delta) = \int_0^\delta \int_0^{\bar{x}} (T_0(\hat{x}) - T_1(\hat{x})) d\hat{x} d\bar{x} = -\left( \nabla T_x - \left\langle \frac{dT_i}{dx} \right\rangle \right) \frac{(L_T - \delta)\delta^2}{2}, \quad (25a)$$

$$F_{12}(\delta) = \int_\delta^{L_T} \int_{\bar{x}}^{L_T} (T_2(\hat{x}) - T_1(\hat{x})) d\hat{x} d\bar{x} = \left( \nabla T_x - \left\langle \frac{dT_i}{dx} \right\rangle \right) \frac{(L_T - \delta)^2 \delta}{2}. \quad (25b)$$

Then, the ensemble-averaged sum of Eqs. (24) takes the form

$$\begin{aligned} \left\langle \frac{dT_i}{dx} \right\rangle &= \frac{\sigma_T}{A_T k_T L_T} \int_0^{L_T} [F_{12}(\delta) - F_{10}(\delta)] d\frac{\delta}{L_T} \\ &= \frac{\text{Bi}}{12} \left( \nabla T_x - \left\langle \frac{dT_i}{dx} \right\rangle \right) \end{aligned} \quad (26)$$

or

$$\left\langle \frac{dT_i}{dx} \right\rangle = \frac{\text{Bi}/12}{1 + \text{Bi}/12} \nabla T_x. \quad (27)$$

Since, according to Eq. (23), the temperature difference does not depend on  $x$ ,  $\langle \bar{Q}_{pair} \rangle$  can be expressed in a form that is similar to Eq. (11)

$$\begin{aligned} \langle \bar{Q}_{pair} \rangle &= -\langle (\delta/L_T)(\bar{T}_1 - \bar{T}_0) \rangle \\ &= -\left( 1 - \frac{\langle dT_i/dx \rangle}{\nabla T_x} \right) \langle \alpha(1 - \alpha) \rangle = -\frac{1/6}{1 + \text{Bi}/12}. \end{aligned} \quad (28)$$

By substituting  $\langle \bar{Q}_{pair} \rangle$  given by Eq. (28) in Eq. (5), we finally find an approximate expression for the bundle conductivity

$$k_{b(app)} = \frac{k_b^0}{1 + \text{Bi}/12}, \quad (29)$$

where

$$k_b^0 = \frac{1}{12} \frac{\sigma_T L_T^2}{A_a} f^0(N_s) \quad (30)$$

is the bundle conductivity at  $\text{Bi} = 0$  given by Eq. (13) at  $\bar{\Delta} = 0$ . In the opposed limit of  $\text{Bi} \rightarrow \infty$ , when the bundle conductivity is dominated by the intrinsic conductivity of CNTs, Eq. (29) reduces to

$$k_b^\infty = k_T \frac{A_T}{A_a} f^0(N_s), \quad (31)$$

where the superscript “ $\infty$ ” marks the case of  $\text{Bi} \rightarrow \infty$ . Thus, Eq. (29) predicts a gradual change in the scaling of the bundle conductivity with the CNT length from  $k \propto L_T^2$  at  $\text{Bi} \ll 1$  to the length-independent  $k_b$  at  $\text{Bi} \gg 1$ .

Although the derivation of  $k_b$  at finite  $\text{Bi}$  discussed above is fairly simple and instructive, it has an apparent flaw related to the fact that the temperature distribution given by Eq. (22) does not satisfy the zero-flux boundary condition on the CNT ends given by Eq. (18b). In order to quantify the applicability of Eq. (29), we compare the predictions of this approximate solution with the accurate analytical solution based on the derivation provided in the Appendix B for a two-axis bundle. As shown in the appendix, the heat flux,  $Q_{pair}$ , for the two-axis system with a given Biot number,  $\text{Bi}$ , and relative displacement of CNT ends,  $\bar{\delta}$ , is given by Eqs. (B22) and (B23). The corresponding ensemble-averaged heat flux,  $\langle Q_{pair} \rangle$ , can then be found as follows:

$$\begin{aligned} \langle \bar{Q}_{pair} \rangle(\text{Bi}) &= 2 \int_0^1 \int_{\bar{x}_1}^1 \frac{Q_{pair}(\text{Bi}, \bar{x}_2 - \bar{x}_1)}{\sigma_T L_T^2 \nabla T_x} d\bar{x}_2 d\bar{x}_1 \\ &= -2 \int_0^1 \int_{\bar{x}_1}^1 \frac{A(\text{Bi}, \bar{x}_2 - \bar{x}_1)}{\text{Bi}} d\bar{x}_2 d\bar{x}_1, \end{aligned} \quad (32)$$

and the averaged conductivity can be represented in the form

$$\bar{k}_b = f^0(N_s) \int_0^1 \int_{\bar{x}_1}^1 \frac{A(\text{Bi}, \bar{x}_2 - \bar{x}_1)}{\text{Bi}} d\bar{x}_2 d\bar{x}_1. \quad (33)$$

In the limits  $\text{Bi} \rightarrow 0$  and  $\text{Bi} \rightarrow \infty$ ,  $k_b$  given by Eq. (33) reduces to  $k_b^0$  and  $k_b^\infty$  given by Eqs. (30) and (31), respectively. Thus, Eqs. (29) and (33) predict the same values in

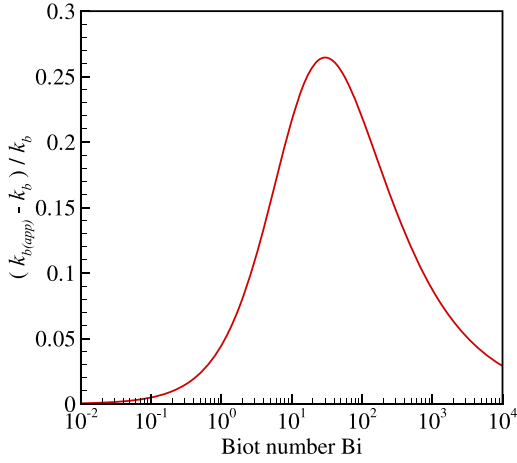


FIG. 10. Relative difference  $(k_{b(app)} - k_b)/k_b$  of thermal conductivities of bundles  $k_{b(app)}$  and  $k_b$  calculated with Eqs. (29) and (33), respectively, plotted as a function of the Biot number  $Bi$ .

the limits of small and large Biot numbers. At finite  $Bi$ , the difference between the predictions of Eqs. (29) and (33) reaches the maximum of  $\sim 27\%$  at  $Bi \approx 30$  and decreases for higher  $Bi$ , as shown in Fig. 10.

### C. Comparison of the theoretical model with numerical results

In order to evaluate the accuracy of the theoretical equations derived above, a series of numerical calculations of the bundle conductivity is performed for  $Bi = 10^{-2} - 10^3$ ,  $0 \leq N_s \leq 4$ ,  $0 \leq \bar{\Delta} \leq 1$ , and  $L_b/L_T = 4$ . Equation (19) is solved iteratively for all nanotubes in a bundle with a tolerance of  $\Delta_Q = 10^{-6}$ . The number of discretization nodes,  $M$ , and the number of random samples,  $N_{sample}$ , used in ensemble averaging of all quantities, including  $\nabla T_x$  and  $k_b$ , are chosen to be  $M = 401$  and  $N_{sample} = 100$ . By varying  $\Delta_Q$ ,  $M$ , and  $N_{sample}$ , it is found that the numerical error in conductivity with these values of numerical parameters is within 1% at  $Bi > 0.1$ , but may increase up to few percentages at  $Bi = 0.01$ .

Typical distributions of temperature along individual CNTs obtained from numerical solution of Eqs. (19) for  $Bi = 1$  and  $Bi = 100$  for a two-axis bundle are shown in Fig. 11 by solid curves. At  $Bi = 1$ , the variation of temperature along a CNT is relatively small. At  $Bi = 100$ , the temperature distribution in an inner part of a CNT is close to linear, but becomes strongly non-linear around the ends where the zero-heat flux conditions, Eq. (18b), are imposed. Even at a large Biot number, e.g.,  $Bi = 100$ , the temperature distribution along a CNT remains quite complex and can only be considered linear as a rough approximation. The theoretical CNT temperature distributions given by Eqs. (B5)–(B8) and shown in Fig. 11 by thick dashed curves are in excellent agreement with the results of the numerical solution of Eq. (19) for finite-length bundles. Since the temperatures of CNTs that cross the boundaries at  $x = 0$  and  $x = L_b$  are not constant, the distribution of the averaged temperature,  $T(x)$ , at large  $Bi$ , e.g., at  $Bi = 100$  (dashed curve in Fig. 7), is close to the linear one,  $\nabla T_x \approx \nabla T_{Bx}$ , and the numerical results are less sensitive to  $L_b$  than in the case  $Bi = 0$ . This weaker

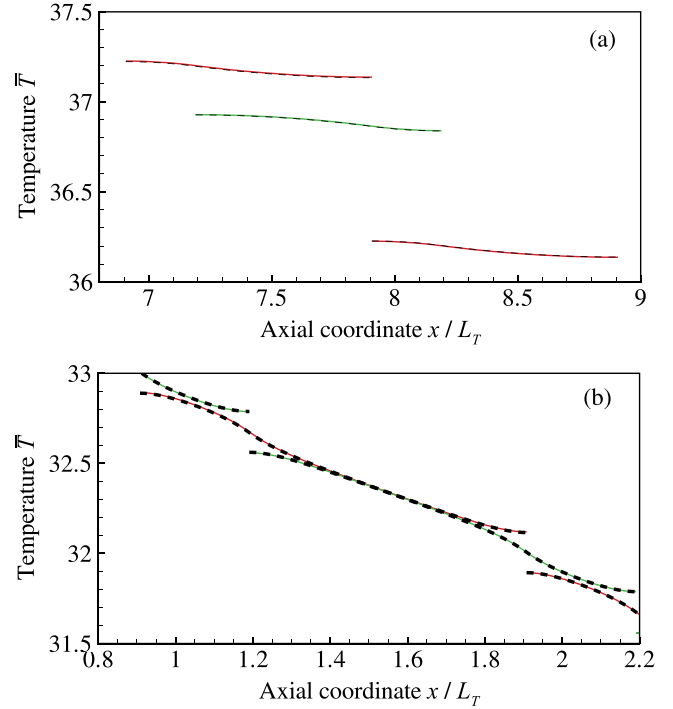


FIG. 11. Typical distributions of temperature along individual CNTs in the central part of a two-axis bundles at  $Bi = 1$  (a) and  $Bi = 100$  (b) at overlap  $\delta/L_T = 0.3$ . Solid curves show distributions found in numerical calculations. Thick dashed curves are the distributions calculated based on analytical solution given by Eqs. (B5)–(B8). The solid and dashed curves visually coincide with each other.

sensitivity to  $L_b$  makes it possible to use shorter bundles in numerical calculations at  $Bi \neq 0$  as compared to the case of  $Bi = 0$ .

Theoretical values of the averaged conductivity calculated based on Eq. (33) for “dense” two-axis bundles (solid curve in Fig. 12(a) for  $\Delta = 0$ ) are in excellent agreement with numerical data (square symbols in Fig. 12(a)) in the whole range of the Biot numbers considered in the calculations. With increasing  $Bi$ , the transition from the scaling law given by Eq. (30) to the scaling law given by Eq. (31) occurs within the transitional range of  $Bi$  from  $10^{-1}$  to  $10^2 - 10^3$ .

In order to calculate the conductivity of two-axis bundles with  $\Delta > 0$ , we multiply values calculated with Eq. (33) by values of the density function given by Eq. (15), i.e., calculate the conductivity with equation

$$\bar{k}_b = f^0(N_s)g(\bar{\Delta}) \int_0^1 \int_0^1 \frac{A(Bi, \bar{x}_2 - \bar{x}_1)}{Bi} d\bar{x}_2 d\bar{x}_1. \quad (34)$$

The results obtained with Eq. (34) (solid curve in Fig. 12(a) for  $\bar{\Delta} = 0.4$ ) are in a fairly good agreement with values of conductivity calculated numerically (triangles in Fig. 12(a)). Thus, for two-axis bundles, the density function given by Eq. (15) provides a good semi-empirical modification of Eq. (33) for the case of  $\Delta > 0$ .

For multi-shell bundles, however, large deviations of the results of numerical calculations from the theoretical predictions of Eq. (33) are observed at large Biot numbers (compare square symbols with dashed curve in Fig. 12(b)). This

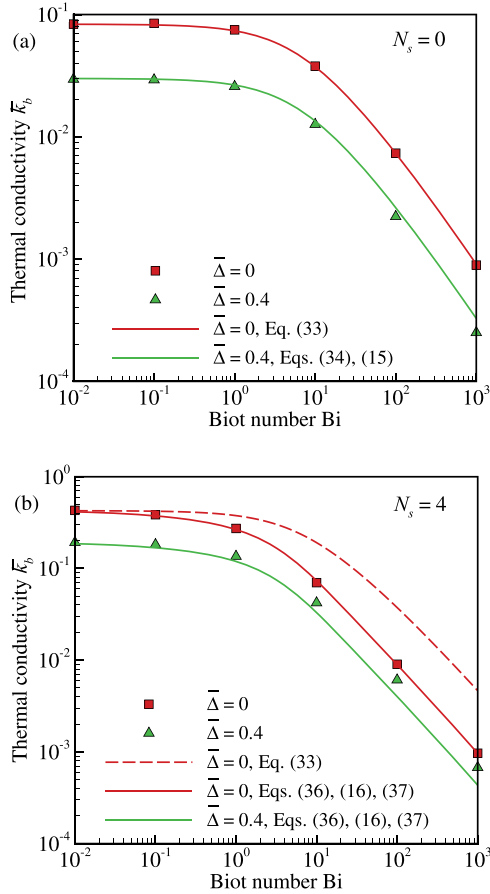


FIG. 12. The ensemble-averaged thermal conductivity,  $\bar{k}_b$ , of two-axis bundles with  $N_s = 0$  (a) and multi-shell bundles with  $N_s = 4$  (b) plotted as a function of Biot number  $Bi$ . Square and triangle symbols represent numerical values calculated for  $\bar{\Delta} = 0$  and  $\bar{\Delta} = 0.4$ , respectively. In panel a, the red curve is obtained with Eq. (33) for  $\bar{\Delta} = 0$  and the green curve is obtained with Eq. (34) for  $\bar{\Delta} = 0.4$ , where the density function is given by Eq. (15). In panel b, the red dashed curve is obtained with Eq. (33) for  $\bar{\Delta} = 0$ , the red and green solid curves are obtained with Eq. (36), where the density and thickness functions are given by Eqs. (16) and (37), at  $\bar{\Delta} = 0$  and  $\bar{\Delta} = 0.4$ , respectively.

deviation can be understood by considering Eq. (27). At  $Bi \rightarrow \infty$ ,  $\langle dT_i/dx \rangle \rightarrow \nabla T_x$  and the averaged heat flux transferred through any axis in the bundle is equal to  $-k_T A_T \nabla T_x$ . The conductivity of the whole bundle is then equal to

$$k_b^\infty = k_T \frac{A_T}{A_a}, \quad (35)$$

i.e., becomes independent of  $N_s$  unlike the prediction based on Eq. (31). The values of the bundle conductivity calculated numerically at large Biot numbers agree perfectly with Eq. (35), suggesting that the theoretical model has to be modified for large  $Bi$  and multi-shell bundles. In Sec. VD, a semi-empirical modification of Eq. (33) that makes it applicable to bundles with arbitrary  $Bi$  and  $N_s$  is proposed.

#### D. Semi-empirical correction of the analytical solution for thermal conductivity at finite Biot number

The discrepancy between the theoretical Eq. (33) and the results of numerical calculations is related to the failure of the equation to account for the transition from the regime

of small  $Bi$ , when the heat flux through a bundle is defined by the inter-tube contact conductance and is proportional to the number of pairs of neighbor axes, to the regime of large  $Bi$ , when the heat flux is defined by the intrinsic conductivity of CNTs and is proportional to the number of axes. In order to account for this transition, one can introduce a new thickness function,  $f(N_s, Bi, \bar{\Delta})$ , so that for a bundle with  $N_s$  shells, conductivity is equal to

$$\bar{k}_b = f(N_s, Bi, \bar{\Delta}) g(\bar{\Delta}) \int_0^1 \int_{\bar{x}_1}^1 \frac{A(Bi, \bar{x}_2 - \bar{x}_1)}{Bi} d\bar{x}_2 d\bar{x}_1. \quad (36)$$

We consider the thickness function  $f(N_s, Bi, \bar{\Delta})$  as a semi-empirical factor in Eq. (36). The values of this function can be calculated numerically as  $f(N_s, Bi, \bar{\Delta}) = k_b(N_s, Bi, \bar{\Delta}) / k_b(0, Bi, \bar{\Delta})$ , where  $k_b(N_s, Bi, \bar{\Delta})$  is the ensemble-averaged conductivity of bundles with given  $N_s$ ,  $Bi$ , and  $\bar{\Delta}$ . Assuming that the primary effect of  $\bar{\Delta}$  on  $\bar{k}_b$  is already accounted for by the density function  $g(\bar{\Delta})$ , the dependence of  $f(N_s, Bi, \bar{\Delta})$  on  $\bar{\Delta}$  can be neglected and, instead of  $f(N_s, Bi, \bar{\Delta})$ , a more simple function,  $f(N_s, Bi) = f(N_s, Bi, 0)$ , can be used in Eq. (36). Numerical values of  $f(N_s, Bi)$ , shown by symbols in Fig. 13 for  $N_s = 1, 2$ , and  $3$ , exhibit smooth variation between the limiting values of  $f^0(N_s)$  at  $Bi \rightarrow 0$  and  $1$  at  $Bi \rightarrow \infty$ . These numerical values of  $f(N_s, Bi)$  can be approximated by a semi-empirical fitting equation

$$f(N_s, Bi) = 1 + \left[ \frac{17}{14} + \left( \frac{f^0(N_s)}{2} - \frac{12}{7} \right) \exp(-0.2\sqrt{Bi}) \right] \times \left\{ 1 + \tanh \left[ -0.79 \log_{10} \left( \frac{Bi}{2.7} \right) \right] \right\}. \quad (37)$$

A good quality of the approximation provided by Eq. (37) can be seen from Fig. 13, where the maximum discrepancy between numerical values (shown by symbols) and the predictions of Eq. (37) (shown by curves) does not exceed 5%. The solid curve in Fig. 13 is calculated based on Eq. (37) in the limit of thick bundles with  $N_s \rightarrow \infty$ . In the case of “dense” bundles with  $\bar{\Delta} = 0$ , values of  $k_b$  calculated based

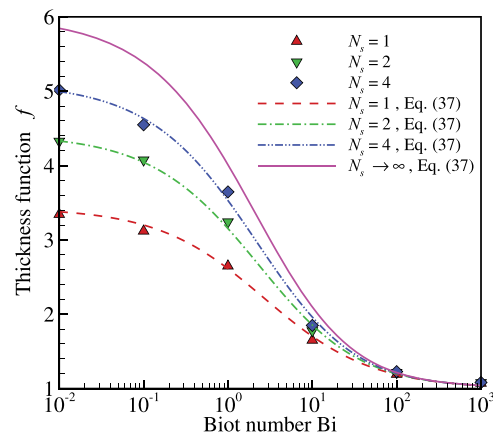


FIG. 13. Thickness function  $f(N_s, Bi)$  versus Biot number  $Bi$  for various  $N_s$ . Symbols represent the values obtained in numerical calculations. Curves are calculated with Eq. (37).

on Eqs. (36) and (37) for thick bundles with  $N_s = 4$  practically coincide with the conductivity found in numerical calculations (red solid curve and square symbols in Fig. 12(b)) in the whole range of Biot numbers considered in the calculations.

In order to calculate the conductivity of thick bundles with  $\bar{\Delta} = 0.4$  based on Eq. (36), we use the density function given by Eq. (16). One can see from Fig. 12(b) (compare solid green curve and triangle symbols) that this approximation provides an accuracy within 10% for  $Bi < 10$ ; while for larger Biot numbers, the deviation of the theoretical curve from the results of numerical calculation is more substantial. One can expect that a more precise semi-empirical approximation of bundle conductivity at finite Biot numbers and large axial separations can be achieved by replacing the factor of 2 under exponent in Eq. (16) by a decreasing function of  $Bi$ .

## VI. THERMAL CONDUCTIVITY OF BUNDLES COMPOSED OF (10,10) CNTs

In this section, we apply Eqs. (36) and (37) for analysis of the conductivity of bundles composed of (10,10) CNTs. The choice of the parameters that define the bundle conductivity is based on the results of atomistic simulations discussed in Sec. II. In particular, the value of inter-tube conductance per unit length,  $\sigma_T = 0.06 \text{ Wm}^{-1}\text{K}^{-1}$  is chosen to match the results shown in Fig. 4.

The choice of the intrinsic thermal conductivity of a CNT is more ambiguous as the values of the conductivity obtained in atomistic simulations vary widely (from tens to thousands of  $\text{Wm}^{-1}\text{K}^{-1}$  for (10,10) CNTs<sup>32,36,37,55,56,66-71</sup>) due to the strong sensitivity of the computational predictions to the CNT length, type of interatomic potential, and other characteristics of the simulation setup.<sup>72</sup> The length dependence of  $k_T$  observed in the simulations is particularly pronounced for  $L_T < 200 \text{ nm}$  and shows signs of saturation at  $L_T \geq 600 \text{ nm}$ .<sup>48,55,66,67,70,71</sup> Indeed, in our simulations performed with the interatomic potential described in Sec. II, a relatively small change of  $k_T$  from  $\sim 223 \text{ Wm}^{-1}\text{K}^{-1}$  to  $\sim 241 \text{ Wm}^{-1}\text{K}^{-1}$  corresponds to the increase of  $L_T$  from 160 to 300 nm (see Table I), which signifies the transition to the diffusive-ballistic regime of phonon transport in CNTs.<sup>47,48,51-53,66,70,71</sup> Further increase of  $L_T$  up to 630 nm results in a moderate additional increase of  $k_T$  up to  $\sim 261 \text{ Wm}^{-1}\text{K}^{-1}$ , while a decrease of  $L_T$  down to 50 nm leads to a more pronounced change in the value of  $k_T$  down to  $\sim 154 \text{ Wm}^{-1}\text{K}^{-1}$ .<sup>72</sup> Using a procedure suggested in Ref. 73, the value of  $k_T$  can be extrapolated to infinite CNT length, yielding  $\sim 277 \text{ Wm}^{-1}\text{K}^{-1}$ .

The interatomic potential is another major factor that affects the values of  $k_T$  predicted in atomistic simulations. By performing simulations with modified AIREBO potential discussed in Sec. II, Brenner potential (REBO),<sup>45</sup> Tersoff potential,<sup>74</sup> and modified Tersoff potential suggested by Lindsay and Broido,<sup>75</sup> we found the values of  $k_T$  ranging from  $\sim 228 \text{ Wm}^{-1}\text{K}^{-1}$  to  $\sim 899 \text{ Wm}^{-1}\text{K}^{-1}$ ,<sup>72</sup> with the latter predicted with the modified Tersoff potential. Given the uncertainty in the precise value of the intrinsic thermal

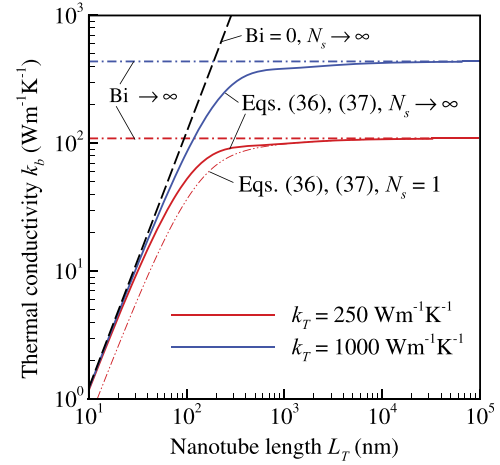


FIG. 14. Thermal conductivity  $k_b$  of bundles of (10,10) CNTs calculated with Eqs. (36) and (37) as a function of the length of individual nanotubes  $L_T$  at  $\Delta = 0$ ,  $\sigma_T = 0.06 \text{ Wm}^{-1}\text{K}^{-1}$ , and two values of thermal conductivities of individual CNTs:  $k_T = 250 \text{ Wm}^{-1}\text{K}^{-1}$  (red curves) and  $k_T = 1000 \text{ Wm}^{-1}\text{K}^{-1}$  (blue curves). Solid, dashed, and dashed-dotted curves are calculated for infinitely thick bundles ( $N_s \rightarrow \infty$ ) at finite  $Bi$ ,  $Bi = 0$ , and  $Bi \rightarrow \infty$ , respectively. The thin dashed-double-dotted curve is obtained for thin bundles,  $N_s = 1$  ( $N_o = 7$ ), at finite  $Bi$ . The geometrical parameters of CNTs used in the calculations are listed in the text.

conductivity of (10,10) CNTs, we perform the analysis of bundle conductivity for two values of  $k_T$ ,  $250 \text{ Wm}^{-1}\text{K}^{-1}$  and  $1000 \text{ Wm}^{-1}\text{K}^{-1}$ . This variation of  $k_T$  also allows us to discuss the sensitivity of the CNT length dependence of the bundle conductivity on the intrinsic conductivity of CNTs. All the geometrical parameters of (10,10) CNTs used in the analysis of bundle conductivity are the same as in Sec. II, i.e.,  $R_T = 0.67 \text{ nm}$ ,  $\delta_T = 0.34 \text{ nm}$ ,  $A_T = 2\pi\delta_T R_T$ , and  $h = 2R_T + \delta_T$ .

The CNT length dependencies of thermal conductivity predicted by Eqs. (36) and (37) for dense, thick bundles ( $\bar{\Delta} = 0$ ,  $N_s \rightarrow \infty$ ) composed of (10,10) CNTs are shown in Fig. 14 for two values of  $k_T$  by the solid curves. The dashed and dashed-dotted curves correspond to the limiting cases of  $Bi = 0$  and  $Bi \rightarrow \infty$ . These results demonstrate that the dependence of the bundle conductivity on the CNT length closely follows the quadratic scaling law only for fairly short nanotubes,  $L_T < L_{T*}$ , where  $L_{T*} \approx 20 \text{ nm}$  at  $k_T = 250 \text{ Wm}^{-1}\text{K}^{-1}$  and  $L_{T*} \approx 40 \text{ nm}$  at  $k_T = 1000 \text{ Wm}^{-1}\text{K}^{-1}$ . In both cases, the value of  $L_{T*}$  roughly corresponds to  $Bi = 0.1$ . For long CNTs, the conductivity of bundles becomes insensitive to the CNT length at  $L_T > L_{T**}$ , where  $L_{T**} = 2 \cdot 10^3 \text{ nm}$  at  $k_T = 250 \text{ Wm}^{-1}\text{K}^{-1}$  and  $L_{T**} = 4 \cdot 10^3 \text{ nm}$  at  $k_T = 1000 \text{ Wm}^{-1}\text{K}^{-1}$ , which roughly corresponds to  $Bi = 10^3$ . In a broad intermediate range of CNT length,  $L_{T*} < L_T < L_{T**}$ , i.e., at  $0.1 < Bi < 10^3$ , the dependence of  $k_b$  on  $L_T$  exhibits a transient behavior between the two limiting cases.

With the change in  $k_T$ , the values of  $L_{T*}$  and  $L_{T**}$  scale as  $L_{T**}, L_{T*} \propto k_T^{1/2}$ . This explains why the range of  $L_T$  that corresponds to the gradual transition between the limiting cases of  $Bi = 0$  and  $Bi \rightarrow \infty$  has relatively weak sensitivity to the value of  $k_T$  assumed in the calculations. For bundles of a finite thickness and  $L_T < L_{T**}$ , the conductivity is smaller than the conductivity of infinitely thick bundles, but the

effect of bundle thickness is limited by a factor of two. This is apparent from the comparison of solid and dash-double-dotted red curves in Fig. 14, where the latter is obtained for bundles composed of seven axis ( $N_S = 1$ ).

Thus, the analysis presented above demonstrates that in a broad range of CNT lengths from  $\sim 20$  nm to  $\sim 4$   $\mu$ m, which is characteristic of many of CNT materials used in current application,<sup>64</sup> the conductivity of CNT bundles has a complex dependence on the thermal properties and length of individual CNTs. For bundles composed of long nanotubes, the thermal conductivity is different from the intrinsic conductivity of individual CNTs by a factor of  $A_T/A_a \sim 1.8\delta_T/R_T$  and is close to the measured conductivity of thin, dense, and well-aligned bundles.<sup>26–28</sup> With decreasing CNT length and, thus, increasing linear density of “free” CNT ends inside bundles, the conductivity drops by orders of magnitude. The complex behavior of the conductivity of CNT bundles in the practically important range of CNT length underlines the importance of the theoretical treatment of the transitional regime characterized by finite values of Biot number.

## VII. SUMMARY

A comprehensive computational and theoretical investigation of the thermal conductivity of CNT bundles is performed to clarify a number of outstanding questions on the mechanisms of heat transfer in a bundle of CNTs arranged into close-packed hexagonal structure and to establish the scaling laws governing the dependence of the bundle conductivity on thermal transport properties of constituent CNTs and structural characteristics of the bundle. The investigation involves two series of atomistic MD simulations, as well as theoretical analysis and numerical modeling performed at the mesoscopic level, i.e., for bundles composed of a large number of CNTs.

The results of MD simulations of thermal conductivity in individual CNTs and in bundles consisting of 2 and 7 CNTs suggest that, contrary to a number of earlier reports, the van der Waals inter-tube coupling in the bundles does not result in any statistically significant changes in the intrinsic conductivity of the CNTs. The simulations of inter-tube heat conduction performed for partially overlapping parallel CNTs indicate that the conductance through the overlap region is proportional to the length of the overlap (the conductance per length is constant) for overlaps that are longer than several tens of nm.

The theoretical analysis and numerical calculations of heat transfer in bundles consisting of CNTs with infinitely large and finite intrinsic thermal conductivity are performed with a mesoscopic model designed based on the results of the MD simulations. The general scaling laws predicting the quadratic dependence of the bundle conductivity on the length of individual CNTs in the case when the thermal transport is controlled by the inter-tube conductance (small Biot number) and the independence of the CNT length in another limiting case when the intrinsic conductivity of CNTs plays the dominant role (large Biot number) are derived. The transition between the two limiting cases is described by a model that combines an analytical core with a few semi-empirical corrections accounting for the correlations between the heat transfer

along different neighboring pairs of axes. In particular, a semi-empirical equation is obtained to describe the gradual change in the dependence of the bundle conductivity on the bundle thickness from the conductivity that is proportional to the number of neighboring pairs of axes in the bundle at small Biot numbers to the conductivity that is proportional to the total number of axes in the bundle at large Biot numbers.

An application of the scaling laws to bundles of single-walled (10,10) CNTs reveals that the transition from inter-tube-conductance-dominated to intrinsic-conductivity-dominated thermal transport in CNT bundles occurs in a practically important range of CNT length from  $\sim 20$  nm to  $\sim 4$   $\mu$ m. In this transitional range, the mesoscopic model predicts a dramatic decrease in the bundle conductivity with decreasing length of individual nanotubes and, thus, with increasing linear density of “free” CNT ends inside bundles. The broad range of CNT length that corresponds to the transition between the two regimes of heat transfer indicates that quantitative analysis of thermal conductivity of CNT bundles cannot rely on simplified scaling laws obtained for the limiting cases of zero or infinite Biot numbers, but should utilize the theoretical description derived in this work for finite values of Biot number.

## ACKNOWLEDGMENTS

Financial support of this work was provided by the National Science Foundation (Grant CBET-1033919) and the Air Force Office of Scientific Research (Award FA9550-10-1-0545). Computational support was provided by the Oak Ridge Leadership Computing Facility (Project MAT048) and the National Science Foundation through the Extreme Science and Engineering Discovery Environment (Project TG-DMR 130010).

## APPENDIX A: ANALYTICAL SOLUTION FOR THE HEAT TRANSFER BETWEEN TWO PARTIALLY OVERLAPPING PARALLEL NANOTUBES

In this appendix, the heat transfer between two partially overlapping parallel CNTs (Fig. 3(a)) is considered and an analytical solution is obtained for temperature distribution in the CNTs. We assume that the overlap region between nanotube 1 and nanotube 2 runs from  $x = a$  to  $x = b = a + \Delta x_{12}$ . Within the overlap region, the steady-state temperature distributions along the two CNTs,  $T_1(x)$  and  $T_2(x)$ , should satisfy the following equations:

$$k_T A_T \frac{d^2 T_1}{dx^2} = \sigma_T (T_1 - T_2), \quad k_T A_T \frac{d^2 T_2}{dx^2} = \sigma_T (T_2 - T_1),$$

$$a \leq x \leq b \quad (\text{A1})$$

where  $k_T$  is the constant intrinsic conductivity of nanotubes,  $\sigma_T$  is the constant contact conductance per unit overlap length, and  $A_T$  is the nanotube cross-sectional area (see Sec. II A). Outside the overlap, the temperature distributions are linear

$$T_1(x) = T_1(a) + \frac{dT_1}{dx} \Big|_{x=a} (x - a), \quad x \leq a, \quad (\text{A2a})$$

$$T_2(x) = T_2(b) + \frac{dT_2}{dx} \Big|_{x=b} (x-b), \quad x \geq b, \quad (\text{A2b})$$

where  $dT_1/dx|_{x \leq a} = dT_2/dx|_{x \geq b} = -Q/(k_T A_T)$  is the temperature gradient along the nanotubes outside the overlap region and  $Q$  is the heat flux through the system ( $Q = Q_{HB}/2$  in Fig. 3).

The general solution of Eqs. (A1) with boundary conditions

$$\frac{dT_1}{dx} \Big|_{x=b} = 0, \quad \frac{dT_2}{dx} \Big|_{x=a} = 0 \quad (\text{A3})$$

takes the following form:

$$T_1(x) = \frac{1}{2} \left( D\bar{x} + E - [C_1 \exp(\sqrt{2\text{Bi}\bar{x}}) + C_2 \exp(-\sqrt{2\text{Bi}\bar{x}})] \right), \quad (\text{A4a})$$

$$T_2(x) = \frac{1}{2} \left( D\bar{x} + E + [C_1 \exp(\sqrt{2\text{Bi}\bar{x}}) + C_2 \exp(-\sqrt{2\text{Bi}\bar{x}})] \right), \quad (\text{A4b})$$

where  $\bar{x} = x/L_T$  and  $\text{Bi} = \sigma_T L_T^2 / (k_T A_T)$ . The constants  $C_1$ ,  $C_2$ ,  $D$ , and  $E$  can be defined in terms of the average temperature,  $T_{12}$ , and the average temperature difference,  $\Delta T_{12}$ , in the overlap region,

$$T_{12} = \frac{1}{\Delta x_{12}} \int_a^b \frac{1}{2} (T_2(x) + T_1(x)) dx, \quad (\text{A5})$$

$$\Delta T_{12} = \frac{1}{\Delta x_{12}} \int_a^b (T_2(x) - T_1(x)) dx,$$

and the parameters that can be directly drawn from the MD simulations. Then,

$$C_1 = -\Delta T_{12} \Delta \bar{x}_{12} \sqrt{2\text{Bi}} \frac{\exp(-\sqrt{2\text{Bi}\bar{a}}) + \exp(-\sqrt{2\text{Bi}\bar{b}})}{4\sinh(\sqrt{2\text{Bi}}\Delta \bar{x}_{12})}, \quad (\text{A6a})$$

$$C_2 = -\Delta T_{12} \Delta \bar{x}_{12} \sqrt{2\text{Bi}} \frac{\exp(\sqrt{2\text{Bi}\bar{a}}) + \exp(\sqrt{2\text{Bi}\bar{b}})}{4\sinh(\sqrt{2\text{Bi}}\Delta \bar{x}_{12})}, \quad (\text{A6b})$$

$$D = -\Delta T_{12} \Delta \bar{x}_{12} \text{Bi}, \quad (\text{A6c})$$

$$E = 2T_{12} - \frac{D(\bar{a} + \bar{b})}{2}, \quad (\text{A6d})$$

where  $\Delta \bar{x}_{12} = \Delta x_{12}/L_T$ ,  $\bar{a} = a/L_T$ , and  $\bar{b} = b/L_T$ . With the assumption of a constant inter-tube conductance per unit overlap length (this assumption is supported by the results of MD simulations presented in Sec. II B), the heat flux through the system can be calculated as

$$Q = \sigma_T \int_a^b (T_2(x) - T_1(x)) dx = \sigma_T \Delta x_{12} \Delta T_{12}. \quad (\text{A7})$$

Thus, in the model based on Eqs. (A1), the conductance averaged over the whole overlap area  $\sigma_{12} = Q/(\Delta x_{12} \Delta T_{12})$  is equal to the ‘‘local’’ conductance  $\sigma_T$ , unless the local conductance depends on the local temperatures of the CNTs.

To compare the temperature profiles predicted by Eqs. (A4) with the results of an MD simulation, these profiles are plotted in Fig. 3(c) for values of  $L_T$ ,  $\Delta x_{12}$ , and  $Q = -Q_{HB}/2$  that are used in the MD simulation illustrated in Fig. 3,  $k_T = 226 \text{ Wm}^{-1} \text{ K}^{-1}$  predicted in MD simulations for  $L_T = 200 \text{ nm}$ , and the time-averaged values of  $T_{12}$  and  $\Delta T_{12}$  drawn from the MD simulation. Based on these parameters, the value of inter-tube conductance  $\sigma_T = 0.06 \text{ Wm}^{-1} \text{ K}^{-1}$  is calculated with Eq. (A7), and all other constants are calculated with Eqs. (A6). The temperature profiles shown in Fig. 3(c) exhibit good agreement between the predictions of the theoretical model and results of MD simulations. This agreement demonstrates that the results of the atomistic simulations of heat transfer between two parallel partially overlapping CNTs can be accurately approximated by the analytical model based on the assumption that the total conductance through the overlap region is proportional to the overlap length.

## APPENDIX B: CONDUCTIVITY OF A TWO-AXIS BUNDLE AT A FINITE BIOT NUMBER

In this appendix, an analytical solution of the problem of conductivity along an infinitely long two-axis bundle is obtained for finite Biot numbers. In order to provide the solution in the simplest mathematical form and to avoid additional complications, only the most important case, when the axial inter-tube separation,  $\Delta$ , is equal to zero, is considered. A unique indexing of CNTs discussed in Sec. III A and illustrated in Fig. 6 for a bundle of finite length is used in the analysis. We assume that  $x = 0$  corresponds to the left end of a CNT with  $k = 1$  located on axis 1, i.e.,  $\delta_1 = 0$ . The relative positions of CNTs on the second axis are then defined by parameter  $\delta (= \delta_2)$ , which is equal to the distance between left ends of CNT 1 on axis 1 and CNT 1 on axis 2. In an infinitely long bundle, the distribution of temperature along different CNTs is a quasi-periodic function of coordinate  $x$ , namely

$$T_k^{(n)}(x) = T_{k-1}^{(n)}(x - L_T) + \nabla T_x L_T, \quad n = 1, 2, \quad (\text{B1})$$

where  $\nabla T_x$  is the imposed temperature gradient along the bundle axis. Thus, it is sufficient to find the temperature distributions along only one CNT on each axis, e.g., CNT 1 on axis 1 and CNT 2 on axis 2. These CNTs are called CNTs 1 and 2 in further discussion and their temperature distributions are denoted as  $T_1(x) = T_1^{(1)}(x)$  and  $T_2(x) = T_2^{(2)}(x)$ .

Our goal is to find  $T_1(x)$  and  $T_2(x)$  for given  $\text{Bi}$  and  $\delta$ . These distributions must satisfy Eq. (17) that also contains temperature distributions  $T_1^{(2)}(x)$  and  $T_2^{(1)}(x)$  of CNTs that have overlaps with CNTs 1 and 2. These temperature distributions, however, can be easily expressed through distributions of temperature in CNTs 1 and 2 by applying Eqs. (B1). Thus, one can write a closed systems of equations with respect to  $T_1(x)$  and  $T_2(x)$ . This system in the dimensionless form can be written as follows:

$$\frac{d^2\bar{T}_1}{d\bar{x}^2} = \text{Bi} \cdot (\bar{T}_1 - \bar{T}_2(\bar{x} + 1) + 1) \quad \text{for } 0 \leq \bar{x} \leq \bar{\delta}, \quad (\text{B2a})$$

$$\frac{d^2\bar{T}_1}{d\bar{x}^2} = \text{Bi} \cdot (\bar{T}_1 - \bar{T}_2), \quad \frac{d^2\bar{T}_2}{d\bar{x}^2} = \text{Bi} \cdot (\bar{T}_2 - \bar{T}_1) \quad \text{for } \bar{\delta} \leq \bar{x} \leq 1, \quad (\text{B2b})$$

$$\frac{d^2\bar{T}_2}{d\bar{x}^2} = \text{Bi} \cdot (\bar{T}_2 - \bar{T}_1(\bar{x} - 1) - 1) \quad \text{for } 1 \leq \bar{x} \leq 1 + \bar{\delta}, \quad (\text{B2c})$$

where  $\bar{\delta} = \delta/L_T$ .

In order to further simplify Eqs. (B2), one can split its solution into two parts, one for  $0 \leq \bar{x} \leq \bar{\delta}$  and another for  $\bar{\delta} \leq \bar{x} \leq 1$ . At  $0 \leq \bar{x} \leq \bar{\delta}$ , we look for the solution in terms of functions  $\bar{T}'_1(\bar{x}) = \bar{T}_1(\bar{x})$  and  $\bar{T}'_2(\bar{x}) = \bar{T}_2(\bar{x} + 1)$ , while keeping the notation  $\bar{T}_1(\bar{x})$  and  $\bar{T}_2(\bar{x})$  for the solution at  $\bar{\delta} \leq \bar{x} \leq 1$ . Then, Eqs. (B2) can be rewritten in the following form:

$$\frac{d^2\bar{T}'_1}{d\bar{x}^2} = \text{Bi} \cdot (\bar{T}'_1 - \bar{T}'_2 + 1), \quad (\text{B3})$$

$$\frac{d^2\bar{T}'_2}{d\bar{x}^2} = \text{Bi} \cdot (\bar{T}'_2 - \bar{T}'_1 - 1) \quad \text{for } 0 \leq \bar{x} \leq \bar{\delta},$$

$$\frac{d^2\bar{T}_1}{d\bar{x}^2} = \text{Bi} \cdot (\bar{T}_1 - \bar{T}_2), \quad \frac{d^2\bar{T}_2}{d\bar{x}^2} = \text{Bi} \cdot (\bar{T}_2 - \bar{T}_1) \quad \text{for } \bar{\delta} \leq \bar{x} \leq 1, \quad (\text{B4})$$

where all functions in all equations are defined at the same point  $\bar{x}$ .

The general solution of Eqs. (B3) can be written in the form

$$\bar{T}'_1(\bar{x}) = \frac{1}{2}(A_1\bar{x} + B_1 - C_1e^{\sqrt{2\text{Bi}}\bar{x}} - D_1e^{-\sqrt{2\text{Bi}}\bar{x}} - 1), \quad (\text{B5})$$

$$\bar{T}'_2(\bar{x}) = \frac{1}{2}(A_1\bar{x} + B_1 + C_1e^{\sqrt{2\text{Bi}}\bar{x}} + D_1e^{-\sqrt{2\text{Bi}}\bar{x}} + 1), \quad (\text{B6})$$

where constants  $A_1$ ,  $B_1$ ,  $C_1$ , and  $D_1$  can be chosen based on appropriate boundary conditions. The general solution of Eqs. (B4) can be written in a similar manner:

$$\bar{T}_1(\bar{x}) = \frac{1}{2}(A_2\bar{x} + B_2 - C_2e^{\sqrt{2\text{Bi}}\bar{x}} - D_2e^{-\sqrt{2\text{Bi}}\bar{x}}), \quad (\text{B7})$$

$$\bar{T}_2(\bar{x}) = \frac{1}{2}(A_2\bar{x} + B_2 + C_2e^{\sqrt{2\text{Bi}}\bar{x}} + D_2e^{-\sqrt{2\text{Bi}}\bar{x}}), \quad (\text{B8})$$

where constants  $A_2$ ,  $B_2$ ,  $C_2$ , and  $D_2$  can be chosen based on appropriate boundary conditions.

In order to find the constants in Eqs. (B5)–(B8), we apply boundary conditions that imply zero derivatives of temperature at all CNT ends and continuity of temperature and its first derivative along the CNTs. These conditions can be written as follows:

$$\left. \frac{d\bar{T}'_1}{d\bar{x}} \right|_{\bar{x}=0} = \left. \frac{d\bar{T}_1}{d\bar{x}} \right|_{\bar{x}=1} = \left. \frac{d\bar{T}'_2}{d\bar{x}} \right|_{\bar{x}=\bar{\delta}} = \left. \frac{d\bar{T}_2}{d\bar{x}} \right|_{\bar{x}=\bar{\delta}} = 0, \quad (\text{B9a})$$

$$\left. \frac{d\bar{T}'_1}{d\bar{x}} \right|_{\bar{x}=\bar{\delta}} = \left. \frac{d\bar{T}_1}{d\bar{x}} \right|_{\bar{x}=\bar{\delta}}, \quad \bar{T}'_1(\bar{\delta}) = \bar{T}_1(\bar{\delta}), \quad (\text{B9b})$$

$$\left. \frac{d\bar{T}'_2}{d\bar{x}} \right|_{\bar{x}=0} = \left. \frac{d\bar{T}_2}{d\bar{x}} \right|_{\bar{x}=1}, \quad \bar{T}'_2(0) = \bar{T}_2(1). \quad (\text{B9c})$$

By inserting Eqs. (B5)–(B8) into conditions given by Eqs. (B9), one can write

$$A_1 - \sqrt{2\text{Bi}}(C_1 - D_1) = 0, \quad (\text{B10})$$

$$A_1 + \sqrt{2\text{Bi}}(C_1e^{\sqrt{2\text{Bi}}\bar{\delta}} - D_1e^{-\sqrt{2\text{Bi}}\bar{\delta}}) = 0, \quad (\text{B11})$$

$$A_2 - \sqrt{2\text{Bi}}(C_2e^{\sqrt{2\text{Bi}}} - D_2e^{-\sqrt{2\text{Bi}}}) = 0, \quad (\text{B12})$$

$$A_2 + \sqrt{2\text{Bi}}(C_2e^{\sqrt{2\text{Bi}}\bar{\delta}} - D_2e^{-\sqrt{2\text{Bi}}\bar{\delta}}) = 0, \quad (\text{B13})$$

$$A_1 - \sqrt{2\text{Bi}}(C_1e^{\sqrt{2\text{Bi}}\bar{\delta}} - D_1e^{-\sqrt{2\text{Bi}}\bar{\delta}}) = A_2 - \sqrt{2\text{Bi}}(C_2e^{\sqrt{2\text{Bi}}\bar{\delta}} - D_2e^{-\sqrt{2\text{Bi}}\bar{\delta}}), \quad (\text{B14})$$

$$A_1\bar{\delta} + B_1 - C_1e^{\sqrt{2\text{Bi}}\bar{\delta}} - D_1e^{-\sqrt{2\text{Bi}}\bar{\delta}} - 1 = A_2\bar{\delta} + B_2 - C_2e^{\sqrt{2\text{Bi}}\bar{\delta}} - D_2e^{-\sqrt{2\text{Bi}}\bar{\delta}}, \quad (\text{B15})$$

$$A_1 + \sqrt{2\text{Bi}}(C_1 - D_1) = A_2 + \sqrt{2\text{Bi}}(C_2e^{\sqrt{2\text{Bi}}} - D_2e^{-\sqrt{2\text{Bi}}}), \quad (\text{B16})$$

$$B_1 + C_1 + D_1 + 1 = A_2 + B_2 + C_2e^{\sqrt{2\text{Bi}}} + D_2e^{-\sqrt{2\text{Bi}}}. \quad (\text{B17})$$

Equation (B14) combined with Eqs. (B11) and (B13) results in  $A_1 = A_2$ . Therefore, we further use notation  $A$  for both  $A_1$  and  $A_2$ . Equation (B16) combined with Eqs. (B10) and (B12) results in the same equation  $A_1 = A_2$ , suggesting that Eqs. (B10)–(B17) represent a degenerated linear system that has an infinitely large number of non-trivial solutions for given values of  $\text{Bi}$  and  $\bar{\delta}$ . In order to find a unique solution of Eqs. (B10)–(B17), one needs to replace Eq. (B14) or Eq. (B16) by an equation that explicitly defines a “reference” value of temperature of a CNT at a particular location along the bundle. For an infinitely long bundle with a quasi-periodic distribution of temperature, the choice of the reference temperature is arbitrary and unavoidably results in a temperature distribution that spans both positive and negative values. For simplicity, we replace Eq. (B16) by the condition  $\bar{T}_1(\bar{\delta}) = 0$ , which results in the following equation:

$$A\bar{\delta} + B_1 - C_1e^{\sqrt{2\text{Bi}}\bar{\delta}} - D_1e^{-\sqrt{2\text{Bi}}\bar{\delta}} - 1 = 0. \quad (\text{B18})$$

Combining this equation with Eq. (B15), one can write

$$A\bar{\delta} + B_2 - C_2e^{\sqrt{2\text{Bi}}\bar{\delta}} - D_2e^{-\sqrt{2\text{Bi}}\bar{\delta}} = 0. \quad (\text{B19})$$

Constants  $C_1$ ,  $D_1$ ,  $C_2$ , and  $D_2$  can be expressed through constant  $A$  from Eqs. (B10)–(B13) as follows:

$$C_1 = -\frac{A}{\sqrt{2\text{Bi}}} \frac{1 + e^{-\sqrt{2\text{Bi}}\bar{\delta}}}{e^{\sqrt{2\text{Bi}}\bar{\delta}} - e^{-\sqrt{2\text{Bi}}\bar{\delta}}}, \quad (\text{B20})$$

$$D_1 = -\frac{A}{\sqrt{2\text{Bi}}} \frac{1 + e^{\sqrt{2\text{Bi}}\bar{\delta}}}{e^{\sqrt{2\text{Bi}}\bar{\delta}} - e^{-\sqrt{2\text{Bi}}\bar{\delta}}},$$

$$C_2 = \frac{A}{\sqrt{2Bi}} \frac{1}{e^{\sqrt{2Bi}} - e^{-\sqrt{2Bi}}}, D_2 = \frac{A}{\sqrt{2Bi}} \frac{1}{e^{\sqrt{2Bi}\delta} - e^{-\sqrt{2Bi}\delta}}. \quad (\text{B21})$$

Constants  $B_1$  and  $B_2$ , in turn, can be expressed through  $A$  by inserting Eqs. (B20) into Eq. (B18) and Eqs. (B21) into Eq. (B19). Finally, the constant  $A$  can be found by inserting Eqs. (B18)–(B21) into Eq. (B17), yielding the following expression:

$$A(\text{Bi}, \bar{\delta}) = 2\sqrt{2\text{Bi}} \left( \sqrt{2\text{Bi}} + 2 \frac{e^{\sqrt{2\text{Bi}\delta}} + e^{-\sqrt{2\text{Bi}\delta}} + 2}{e^{\sqrt{2\text{Bi}\delta}} - e^{-\sqrt{2\text{Bi}\delta}}} + 2 \frac{e^{\sqrt{2\text{Bi}(1-\bar{\delta})}} - e^{-\sqrt{2\text{Bi}(1-\bar{\delta})}}}{e^{\sqrt{2\text{Bi}(1-\bar{\delta})}} + e^{-\sqrt{2\text{Bi}(1-\bar{\delta})}} - 2} \right)^{-1}. \quad (\text{B22})$$

Thus, Eqs. (B5)–(B8), where constants are defined by Eqs. (B18)–(B22), enable calculation of temperature distribution in any CNT that belong to an infinitely long two-axis bundle for given values of  $\text{Bi}$  and  $\bar{\delta}$ .

The heat flux,  $Q_{\text{pair}}$ , propagating through the bundle can be calculated in a number of different ways, e.g., as  $Q_{\text{pair}} = -k_T A_T dT_1/dx|_{x=\delta}$  or  $Q_{\text{pair}} = \sigma_T \int_{\delta}^{L_T} (T_1 - T_2) dx$ , which yields the same result

$$Q_{\text{pair}} = -\sigma_T L_T^2 \nabla T_x \frac{A(\text{Bi}, \bar{\delta})}{\text{Bi}}. \quad (\text{B23})$$

- <sup>1</sup>P. Kim, L. Shi, A. Majumdar, and P. L. McEuen, “Thermal transport measurements of individual multiwalled nanotubes,” *Phys. Rev. Lett.* **87**, 215502 (2001).
- <sup>2</sup>M. Fujii, X. Zhang, H. Xie, H. Ago, K. Takahashi, T. Ikuta, H. Abe, and T. Shimizu, “Measuring the thermal conductivity of a single carbon nanotube,” *Phys. Rev. Lett.* **95**, 065502 (2005).
- <sup>3</sup>E. Pop, D. Mann, Q. Wang, K. Goodson, and H. Dai, “Thermal conductance of an individual single-wall carbon nanotube above room temperature,” *Nano Lett.* **6**, 96–100 (2006).
- <sup>4</sup>Q. Li, C. Liu, X. Wang, and S. Fan, “Measuring the thermal conductivity of individual carbon nanotubes by the Raman shift method,” *Nanotechnology* **20**, 145702 (2009).
- <sup>5</sup>A. A. Balandin, “Thermal properties of graphene and nanostructured carbon materials,” *Nature Mater.* **10**, 569–581 (2011).
- <sup>6</sup>A. M. Marconnet, M. A. Panzer, and K. E. Goodson, “Thermal conduction phenomena in carbon nanotubes and related nanostructured materials,” *Rev. Mod. Phys.* **85**, 1295–1326 (2013).
- <sup>7</sup>R. Cross, B. A. Cola, T. Fisher, X. Xu, K. Gall, and S. Graham, “A metallization and bonding approach for high performance carbon nanotube thermal interface materials,” *Nanotechnology* **21**, 445705 (2010).
- <sup>8</sup>H. M. Duong and S. T. Nguyen, “Limiting mechanisms of thermal transport in carbon nanotube-based heterogeneous media,” *Recent Patents Eng.* **5**, 209–232 (2011).
- <sup>9</sup>K. Kordás, G. Tóth, P. Moilanen, M. Kumpumäki, J. Vähäkangas, A. Uusimäki, R. Vajtai, and P. M. Ajayan, “Chip cooling with integrated carbon nanotube microfin architectures,” *Appl. Phys. Lett.* **90**, 123105 (2007).
- <sup>10</sup>Y. Fu, N. Nabiollahi, T. Wang, S. Wang, Z. Hu, B. Carlberg, Y. Zhang, X. Wang, and J. Liu, “A complete carbon-nanotube-based on-chip cooling solution with very high heat dissipation capacity,” *Nanotechnology* **23**, 045304 (2012).
- <sup>11</sup>A. Thess, R. Lee, P. Nikolaev, H. Dai, P. Petit, J. Robert, C. Xu, Y. H. Lee, S. G. Kim, A. G. Rinzler, D. T. Colbert, G. E. Scuseria, D. Tománek, J. E. Fischer, and R. E. Smalley, “Crystalline ropes of metallic carbon nanotubes,” *Science* **273**, 483–487 (1996).

- <sup>12</sup>A. G. Rinzler, J. Liu, H. Dai, P. Nikolaev, C. B. Huffman, F. J. Rodríguez-Macias, P. J. Boul, A. H. Lu, D. Heymann, D. T. Colbert, R. S. Lee, J. E. Fischer, A. M. Rao, P. C. Eklund, and R. E. Smalley, “Large-scale purification of single-wall carbon nanotubes: Process, product, and characterization,” *Appl. Phys. A: Mater. Sci. Process.* **67**, 29–37 (1998).
- <sup>13</sup>W. Ma, L. Song, R. Yang, T. Zhang, Y. Zhao, L. Sun, Y. Ren, D. Liu, L. Liu, J. Shen, Z. Zhang, Y. Xiang, W. Zhou, and S. Xie, “Directly synthesized strong, highly conducting, transparent single-walled carbon nanotube films,” *Nano Lett.* **7**, 2307–2311 (2007).
- <sup>14</sup>S. Wang, Z. Liang, B. Wang, and C. Zhang, “High-strength and multifunctional macroscopic fabric of single-walled carbon nanotubes,” *Adv. Mater.* **19**, 1257–1261 (2007).
- <sup>15</sup>F. Hennrich, S. Lebedkin, S. Malik, J. Tracy, M. Barczewski, H. Rösner, and M. Kappes, “Preparation, characterization and applications of free-standing single walled carbon nanotube thin films,” *Phys. Chem. Chem. Phys.* **4**, 2273–2277 (2002).
- <sup>16</sup>H. Chen, M. Chen, J. Di, G. Xu, H. Li, and Q. Li, “Architecting three-dimensional networks in carbon nanotube buckypapers for thermal interface materials,” *J. Phys. Chem. C* **116**, 3903–3909 (2012).
- <sup>17</sup>A. N. Volkov and L. V. Zhigilei, “Structural stability of carbon nanotube films: The role of bending buckling,” *ACS Nano* **4**, 6187–6195 (2010).
- <sup>18</sup>L. V. Zhigilei, C. Wei, and D. Srivastava, “Mesoscopic model for dynamic simulations of carbon nanotubes,” *Phys. Rev. B* **71**, 165417 (2005).
- <sup>19</sup>A. N. Volkov and L. V. Zhigilei, “Mesoscopic interaction potential for carbon nanotubes of arbitrary length and orientation,” *J. Phys. Chem. C* **114**, 5513–5531 (2010).
- <sup>20</sup>M. Monthioux, B. W. Smith, B. Burtiaux, A. Claye, J. E. Fischer, and D. E. Luzzi, “Sensitivity of single-wall carbon nanotubes to chemical processing: An electron microscopy investigation,” *Carbon* **39**, 1251–1272 (2001).
- <sup>21</sup>A. N. Volkov and L. V. Zhigilei, “Scaling laws and mesoscopic modeling of thermal conductivity in carbon nanotube materials,” *Phys. Rev. Lett.* **104**, 215902 (2010).
- <sup>22</sup>T. Xu, Z. Wang, J. Miao, X. Chen, and C. M. Tan, “Aligned carbon nanotubes for through-wafer interconnects,” *Appl. Phys. Lett.* **91**, 042108 (2007).
- <sup>23</sup>T. Wang, K. Jeppson, L. Ye, and J. Liu, “Carbon-nanotube through-silicon via interconnects for three-dimensional integration,” *Small* **7**, 2313–2317 (2011).
- <sup>24</sup>J. Hou, X. Wang, P. Vellecheruvu, J. Guo, C. Liu, and H.-M. Cheng, “Thermal characterization of single-wall carbon nanotube bundles using the self-heating  $3\omega$  technique,” *J. Appl. Phys.* **100**, 124314 (2006).
- <sup>25</sup>X. Huang, J. Wang, G. Eres, and X. Wang, “Thermophysical properties of multi-wall carbon nanotube bundles at elevated temperatures up to 830 K,” *Carbon* **49**, 1680–1691 (2011).
- <sup>26</sup>I. K. Hsu, M. T. Pettes, A. Bushmaker, M. Aykol, L. Shi, and S. B. Cronin, “Optical absorption and thermal transport of individual suspended carbon nanotube bundles,” *Nano Lett.* **9**, 590–594 (2009).
- <sup>27</sup>I.-K. Hsu, M. T. Pettes, M. Aykol, C.-C. Chang, W.-H. Hung, J. Theiss, L. Shi, and S. B. Cronin, “Direct observation of heat dissipation in individual suspended carbon nanotubes using a two-laser technique,” *J. Appl. Phys.* **110**, 044328 (2011).
- <sup>28</sup>L. Shi, D. Li, C. Yu, W. Jang, D. Kim, Z. Yao, P. Kim, and A. Majumdar, “Measuring thermal and thermoelectric properties of one-dimensional nanostructures using a microfabricated device,” *Trans. ASME Ser. C: J. Heat Transfer* **125**, 881–888 (2003).
- <sup>29</sup>A. E. Aliev, M. H. Lima, E. M. Silverman, and R. H. Baughman, “Thermal conductivity of multi-walled carbon nanotube sheets: Radiation losses and quenching of phonon modes,” *Nanotechnology* **21**, 035709 (2010).
- <sup>30</sup>W. Lin, J. Shang, W. Gu, and C. P. Wong, “Parametric study of intrinsic thermal transport in vertically aligned multi-walled carbon nanotubes using a laser flash technique,” *Carbon* **50**, 1591–1603 (2012).
- <sup>31</sup>J. Hone, M. C. Llaguno, M. J. Biercuk, A. T. Johnson, B. Batlogg, Z. Benes, and J. E. Fischer, “Thermal properties of carbon nanotubes and nanotube-based materials,” *Appl. Phys. A* **74**, 339–343 (2002).
- <sup>32</sup>S. Berber, Y.-K. Kwon, and D. Tománek, “Unusually high thermal conductivity of carbon nanotubes,” *Phys. Rev. Lett.* **84**, 4613–4616 (2000).
- <sup>33</sup>J. Yang, Y. Yang, S. W. Walthermire, X. Wu, H. Zhang, T. Gutu, Y. Jiang, Y. Chen, A. A. Zinn, R. Prasher, T. T. Xu, and D. Li, “Enhanced and switchable nanoscale thermal conduction due to van der Waals interfaces,” *Nat. Nanotech.* **7**, 91–95 (2012).
- <sup>34</sup>X. H. Yan, Y. Xiao, and Z. M. Li, “Effects of intertube coupling and tube chirality on thermal transport of carbon nanotubes,” *J. Appl. Phys.* **99**, 124305 (2006).

- <sup>35</sup>J. Yang, S. Waltermire, Y. Chen, A. A. Zinn, T. T. Xu, and D. Li, "Contact thermal resistance between individual multiwall carbon nanotubes," *Appl. Phys. Lett.* **96**, 023109 (2010).
- <sup>36</sup>H. Zhong and J. R. Lukes, "Interfacial thermal resistance between carbon nanotubes: Molecular dynamics simulations and analytical thermal modeling," *Phys. Rev. B* **74**, 125403 (2006).
- <sup>37</sup>S. Maruyama, Y. Igarashi, Y. Taniguchi, and J. Shiomi, "Anisotropic heat transfer of single-walled carbon nanotubes," *J. Thermal Sci. Technol.* **1**, 138–148 (2006).
- <sup>38</sup>Z. Xu and M. J. Buehler, "Nanoengineering heat transfer performance at carbon nanotube interfaces," *ACS Nano* **3**, 2767–2775 (2009).
- <sup>39</sup>V. Varshney, S. S. Patnaik, A. K. Roy, and B. L. Farmer, "Modeling of thermal conductance at transverse CNT-CNT interfaces," *J. Phys. Chem. C* **114**, 16223–16228 (2010).
- <sup>40</sup>Y. Chalopin, S. Volz, and N. Mingo, "Upper bound to the thermal conductivity of carbon nanotube pellets," *J. Appl. Phys.* **105**, 084301 (2009).
- <sup>41</sup>R. S. Prasher, X. J. Hu, Y. Chalopin, N. Mingo, K. Lofgreen, S. Volz, F. Cleri, and P. Keblinski, "Turning carbon nanotubes from exceptional heat conductors into insulators," *Phys. Rev. Lett.* **102**, 105901 (2009).
- <sup>42</sup>W. J. Evans, M. Shen, and P. Keblinski, "Inter-tube thermal conductance in carbon nanotubes arrays and bundles: Effects of contact area and pressure," *Appl. Phys. Lett.* **100**, 261908 (2012).
- <sup>43</sup>S. Plimpton, "Fast parallel algorithms for short-range molecular dynamics," *J. Comput. Phys.* **117**, 1–19 (1995).
- <sup>44</sup>S. J. Stuart, A. B. Tutein, and J. A. Harrison, "A reactive potential for hydrocarbons with intermolecular interactions," *J. Chem. Phys.* **112**, 6472–6486 (2000).
- <sup>45</sup>D. W. Brenner, O. A. Shenderova, J. A. Harrison, S. J. Stuart, B. Ni, and S. B. Sinnott, "A second-generation reactive empirical bond order (REBO) potential energy expression for hydrocarbons," *J. Phys.: Condens. Matter* **14**, 783–802 (2002).
- <sup>46</sup>The cutoff of the nonbonding interaction potential at large distances is not explicitly discussed in Ref. 44 but is used in the computational code implementing the AIREBO potential and provided to us by Steven Stuart of Clemson University. The values of  $2.16\sigma$  to  $3\sigma$  are from the code.
- <sup>47</sup>J. R. Lukes and H. Zhong, "Thermal conductivity of individual single-wall carbon nanotubes," *J. Heat Transfer* **129**, 705–716 (2007).
- <sup>48</sup>S. Maruyama, "A molecular dynamics simulation of heat conduction in finite length SWNTs," *Physica B* **323**, 193–195 (2002).
- <sup>49</sup>A. N. Volkov and L. V. Zhigilei, "Heat conduction in carbon nanotube materials: Strong effect of intrinsic thermal conductivity of carbon nanotubes," *Appl. Phys. Lett.* **101**, 043113 (2012).
- <sup>50</sup>A. N. Volkov, T. Shiga, D. Nicholson, J. Shiomi, and L. V. Zhigilei, "Effect of bending buckling of carbon nanotubes on thermal conductivity of carbon nanotube materials," *J. Appl. Phys.* **111**, 053501 (2012).
- <sup>51</sup>J. Wang and J.-S. Wang, "Carbon nanotube thermal transport: Ballistic to diffusive," *Appl. Phys. Lett.* **88**, 111909 (2006).
- <sup>52</sup>J. Shiomi and S. Maruyama, "Molecular dynamics of diffusive-ballistic heat conduction in single-walled carbon nanotubes," *Jpn. J. Appl. Phys.* **47**, 2005–2009 (2008).
- <sup>53</sup>N. Mingo and D. A. Broido, "Carbon nanotube ballistic thermal conductance and its limits," *Phys. Rev. Lett.* **95**, 096105 (2005).
- <sup>54</sup>M. S. Dresselhaus and P. C. Eklund, "Phonons in carbon nanotubes," *Adv. Phys.* **49**, 705–814 (2000).
- <sup>55</sup>J. F. Moreland, J. B. Freund, and G. Chen, "The disparate thermal conductivity of carbon nanotubes and diamond nanowires studied by atomistic simulations," *Microscale Thermophys. Eng.* **8**, 61–69 (2004).
- <sup>56</sup>M. Grujicic, G. Cao, and B. Gersten, "Atomic-scale computations of the lattice contribution to thermal conductivity of single-walled carbon nanotubes," *Mater. Sci. Eng. B* **107**, 204–216 (2004).
- <sup>57</sup>The values of interface conductance given in Ref. 39 in units of  $\text{Wm}^{-1}\text{K}^{-1}$  (Figs. 6 and 7 of Ref. 39) are about an order of magnitude larger than the actual values found in the simulations, as established through private communication with Dr. Vikas Varshney.
- <sup>58</sup>The values of the thermal boundary conductance between CNTs in a bundle reported in Table IV of Ref. 37 are twice smaller than its actual value found in the simulations and the value of the surface area is twice higher than the value reported in this table, as established through private communication with Professor Junichiro Shiomi. The conductance in units of  $\text{WK}^{-1}$  or  $\text{WK}^{-1}\text{m}^{-1}$ , however, is not affected by these corrections.
- <sup>59</sup>S. T. Huxtable, D. G. Cahill, S. Shenogin, L. Xue, R. Ozisik, P. Barone, M. Usrey, M. S. Strano, G. Siddons, M. Shim, and P. Keblinski, "Interfacial heat flow in carbon nanotube suspensions," *Nature Mater.* **2**, 731–734 (2003).
- <sup>60</sup>E. Pop, D. A. Mann, K. E. Goodson, and H. Dai, "Electrical and thermal transport in metallic single-wall carbon nanotubes on insulating substrates," *J. Appl. Phys.* **101**, 093710 (2007).
- <sup>61</sup>L. I. Sedov, *Similarity and Dimensional Methods in Mechanics* (CRC Press, Boca Raton, 1993).
- <sup>62</sup>F. Kreith and M. S. Bohn, *Principles of Heat Transfer*, 6th ed. (Brooks/Cole Pub., Pacific Grove, 2001).
- <sup>63</sup>S. V. Patankar, *Numerical Heat Transfer and Fluid Flow* (Hemisphere, New York, 1980).
- <sup>64</sup>W. Bauhofer and J. Z. Kovacs, "A review and analysis of electrical percolation in carbon nanotube polymer composites," *Compos. Sci. Technol.* **69**, 1486–1498 (2009).
- <sup>65</sup>A. N. Volkov and L. V. Zhigilei, "Thermal conductivity of two-dimensional disordered fibrous materials governed by thermal contact resistance" (unpublished).
- <sup>66</sup>S. Maruyama, "A molecular dynamics simulation of heat conduction of a finite length single-walled carbon nanotube," *Microscale Thermophys. Eng.* **7**, 41–50 (2003).
- <sup>67</sup>C. W. Padgett and D. W. Brenner, "Influence of chemisorption on the thermal conductivity of single-wall carbon nanotubes," *Nano Lett.* **4**, 1051–1053 (2004).
- <sup>68</sup>G. Zhang and B. Li, "Thermal conductivity of nanotubes revisited: Effects of chirality, isotope impurity, tube length, and temperature," *J. Chem. Phys.* **123**, 114714 (2005).
- <sup>69</sup>Z. Xu and M. J. Buehler, "Strain controlled thermomutability of single-walled carbon nanotubes," *Nanotechnology* **20**, 185701 (2009).
- <sup>70</sup>J. A. Thomas, R. M. Iutzi, and A. J. McGaughey, "Thermal conductivity and phonon transport in empty and water-filled carbon nanotubes," *Phys. Rev. B* **81**, 045413 (2010).
- <sup>71</sup>A. Cao and J. Qu, "Size dependent thermal conductivity of single-walled carbon nanotubes," *J. Appl. Phys.* **112**, 013503 (2012).
- <sup>72</sup>R. N. Salaway and L. V. Zhigilei, "Molecular dynamics simulations of thermal conductivity of carbon nanotubes: Resolving the effect of computational parameters" (unpublished).
- <sup>73</sup>P. K. Schelling, S. R. Phillpot, and P. Keblinski, "Comparison of atomic-level simulation methods for computing thermal conductivity," *Phys. Rev. B* **65**, 144306 (2002).
- <sup>74</sup>J. Tersoff, "Empirical interatomic potential for carbon, with applications to amorphous carbon," *Phys. Rev. Lett.* **61**, 2879–2882 (1988).
- <sup>75</sup>L. Lindsay and D. A. Broido, "Optimized Tersoff and Brenner empirical potential parameters for lattice dynamics and phonon thermal transport in carbon nanotubes and graphene," *Phys. Rev. B* **81**, 205441 (2010).